STUDIA UNIVERSITATIS
BABEŞ-BOLYAI

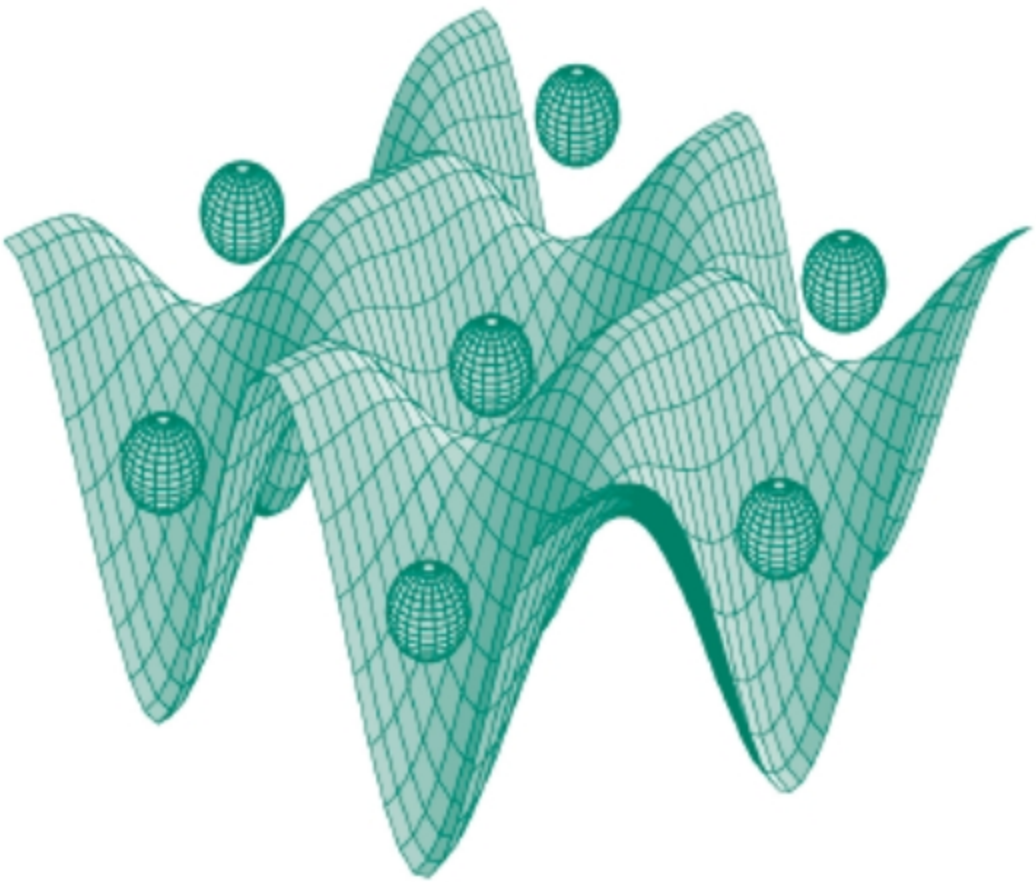

PHYSICA

2/2007

ANUL LII **2007**

S T U D I A
UNIVERSITATIS BABEŞ-BOLYAI

PHYSICA

2

EDITORIAL OFFICE: Haşdeu no. 51, 400371 Cluj-Napoca ♦ Phone 0264-40.53.52

CUPRINS - CONTENTS - SOMMAIRE

ARANKA DERZSI, Complex Spatial Model for Macroecological Patterns..... 3
M. BODEA, P. BALINT, T. R. YANG, A.V. POP, C. LUNG, G. ILONCA, Transport Phenomena and Ac-Susceptibility of (Bi;Pb):2223 Superconductors Doped with Sm Ions..... 15
CRISTINA M. MUNTEAN, ANDREI IOACHIM, DUMITRU MOLDOVEANU, Microwave Absorption in Chromosomal DNA Molecules 23
LÓRÁND HORVÁTH, TITUS A. BEU, Tight-Binding Molecular Dynamics Simulations of Radiation Induced Fragmentation of C_{60}..... 35
KLÁRA MAGYARI, ZOLTÁN BÁLINT, VIORICA SIMON, GYÖRGY VÁRÓ, Spectroscopic and Electric Signal Measurements of the Retinal Reconstituted Bacteriorhodopsin..... 47

R. I. CAMPEANU, Electron Impact Ionization of Kr and Xe 55
S. SIMON, H. MOCUTA, M. BĂCIUŢ, G. BĂCIUŢ, V. COMAN, P. PRODAN, ŞT. I. FLORIAN, Heat Treatment Effect on Nanocrystalline Mineral Phase of Bones 63
O. PONTA, D. A. UDVAR, S. SIMON, Structural Characterisation of Gadolinium Doped $0.875Bi_2O_30.125GeO_2$ Non- and Polycrystalline System 71
I. GROSU, L.TUGULAN, Electron Density Oscillations in one-dimension for a Chain of Dense Impurities 79

STUDIA UNIVERSITATIS BABEŞ-BOLYAI, PHYSICA, LII, 2, 2007

COMPLEX SPATIAL MODEL FOR MACROECOLOGICAL PATTERNS

ARANKA DERZSI*

ABSTRACT. A complex spatially extended model is introduced in order to study the species abundances distribution, the species-area relation and the spatial distribution of species in neutral ecological communities. Computer simulation results are treated in comparison with measured data on a large-scale neutral type ecological system. The main features of the related neutral community simulator software are presented and the obtained results are critically discussed.

1. Introduction

Neutral theory is a much-debated hypothesis that aims to explain the observed patterns of species abundances, distribution and diversity in certain ecological communities. This approach, introduced by S. Hubbel [1-2], comes against the widely established niche-based explanations [3]. Neutral theory assumes the equality of all species in the community in the sense that they all possess similar birth and death rates and compete with each other only for the limited amount of resources. In such communities randomness has the key role in determining the dynamics and species composition of the system, allowing the alternation of dominant species too. By means of random processes, the number of individuals in various species are fluctuating and forming a peculiar and somehow universal species abundance distribution. The neutral model elaborated by Hubbel [2] reproduces surprisingly well the observed patterns of species abundances, offering thus a strong foundation for further neutral ecological modeling. The nowadays used mean-field type variants of the model reproduce nicely the experimentally observed relative species abundances but there are serious shortcomings in describing the species-area scaling and the spatial distribution of species [4-7]. The aim of the present work is to introduce a complex spatially extended neutral community model which is able to describe all the major statistical aspects of neutral systems.

* Babeş-Bolyai University, Department of Theoretical and Computational Physics, str. Kogalniceanu 1., RO-400084, Cluj-Napoca, Romania, Email: aderzsi@phys.ubbcluj.ro

2. Experimental data – Barro Colorado Island data set

The Smithsonian Tropical Research Institute (STRI) maintains extensive research of rainforest ecosystems in various spots of the world and creates ample experimental databases regarding the species diversity and distribution in the mapped regions. One of the STRI's permanent research centers is established on the Barro Colorado Island (BCI) located in the Panama Canal waterway. To document the changes in the species composition, trees are sampled in a 50-ha region of the island from 1983, re-censuses occurring every 5 years since. This data set provides large scale statistical data both on species abundances and their spatial distribution. Assuming that communities of tropical trees are good examples of neutral ecosystems, the BCI database is a great experimental reference for testing the adequacy of neutral ecological models.

Ecologists usually investigate the relative species abundances (RSA), the species spatial distribution in a given ecosystem. A generally accepted method for representing RSA is the Preston-type plot, obtained by considering abundances intervals with exponentially increasing length and counting the number of species with sizes found within these intervals. Dividing the number of species in each interval by the length of the interval and the total number of species yields a mathematically more rigorous RSA representation: the probability density of finding a species with a given abundance. In case of the BCI data set, as well as in widely different communities, the Preston-type representation of species abundances has a Gaussian shape [8] and the probability density function follows a power-low curve with exponent around -1 in the limit of rare species. In the limit of the abundant species the RSA curve has an exponential cutoff. The cumulative number of species recorded in areas of successively larger sizes plotted agains the size of the area, constitutes the species-area curve. This curve has a scaling behavior with exponents between 0.2-0.5. The autocorrelation function of the individuals in given species, characterizes the spatial distribution of a given species of the community. Experimental results from BCI indicate that the auto-correlation function exhibits also a scaling behavior for abundant species [9]. Successful models for biodiversity should reproduce both the species abundances distribution and the measured spatial scaling laws. In trying to accomplish this task, we have elaborated a complex and realistic spatially extended model which is presented briefly in the next section.

3. A spatially extended neutral community model

Our complex model is defined on a square lattice. Each lattice site can be occupied by many individuals belonging to different species. In this manner a lattice site corresponds to a sub-region of the modeled territory. The total number of individuals for each lattice site can fluctuate around a given

N_0 value. This parameter characterizes the carrying capacity of the related sub-territories. Accordingly, the lattice sites stand for sub-territories possessing not necessarily equal areas but the same amount of available resources.

The dynamics of the system is governed by birth, death and migration processes. In reality, the available amount of resources determines the variation of the birth/death ratio. The overpopulation of a territory will generate lack of resources, consequently increase of mortality, while the abundance of resources enhance multiplication. Given a territory with fixed carrying capacity, the number of individuals in it controls the proportion of birth and death processes. Since in the considered model lattice sites represent sub-territories with the same carrying capacity but not necessarily the same number of individuals, they should have different birth/death ratio too. For this reason the d death rate is defined as function of the number of individuals (N) ensuring a proper death rates for each lattice site. The death-rate function is given by the following relation:

$$d(N) = 1 - \frac{1 - d_0}{e^{\frac{N - N_0}{\alpha}} + 1} \qquad (1.)$$

where d_0 is a fixed death rate that stands for the $N = 1$ particular case and N_0>>1 is the carrying capacity of the sub-territory. The α parameter controls the steepness of the death-rate curve. Figure 1. presents this curve for various values of α. According to the relation above, $d(N)$ exhibits a considerable increase in the neighborhood of N_0.

Within our model the b multiplication rate is considered the same for each lattice site. The birth process includes also the chance of origination of a new species by mutation. This can happened with a probability m whenever a multiplication is considered. Individuals from an external metacommunity are also allowed to come into the system with a w immigration probability. Beside mutation, the immigration process can also introduce new species into the system. The spatiality of the model implies considering also the realistic spatial movement of individuals. This process is characterized by a q migration rate.

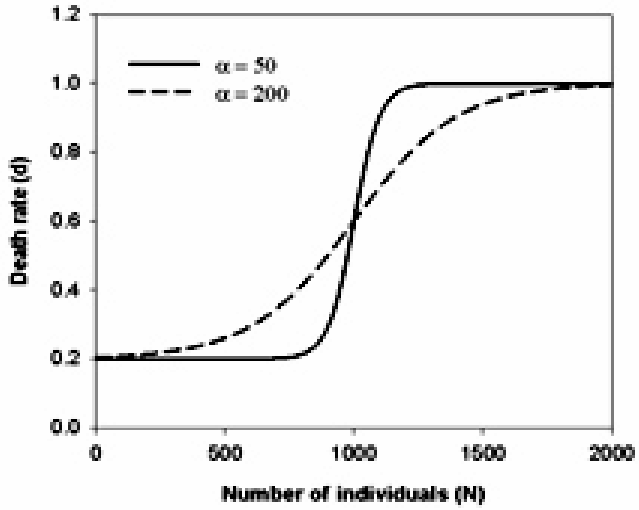

Figure 1. The $d(N)$ death-rate function plotted for $\alpha = 50$ (continuous line) and $\alpha = 200$ (dashed line). The other parameters of the function: $d_0 = 0.2$, $N_0 = 1000$

On account of the model's neutrality, all individuals, regardless of their species, have the same d_0, α., b, m, w and q parameters. The initialization of the system consists in the definition of these parameters together with the characteristics of the lattice: the size of the lattice, the N_0 carrying capacity of the lattice sites, and the number of different species. The initialization of the system completes with assigning a specified number of individuals from randomly selected species to randomly chosen lattice sites.

The dynamics of the considered neutral community model is than straightforward:

- Time is updated by small steps
- In each time-step for all individuals we consider all the possible processes that have nonzero rates: individuals can give birth to another individual (which can belong to the same species or to a new species originated by mutation), can die or can migrate to one of the four neighbour sites. With the initially fixed rates, an individual from the external metacommunity can be also assigned to a randomly chosen lattice site.
- The death rates are recalculated for those lattice sites on which the number of individuals got changed and a new time-step considered.

The considered dynamics can be efficiently implemented by using a kinetic Monte Carlo method and considering periodic boundary conditions. Based on this complex spatial model, we have developed two user-friendly and interactive programs which investigate the evolution and statistical properties of neutral-like ecological communities. The next section provides a detailed presentation of the operation and built-in functionalities of these applications.

4. The Neutral Community Simulator

The program package designed for the study of neutral communities contains two complementary applications: the first (*Simulation*) realizes an interactive simulation of the complex spatially extended model while the second (*Data analysis*) statistically processes the output data of the simulations [10].

Simulation: In the application's window (Figure 2) one can specify the parameters of the model: the size of the lattice, the initial number of individuals, the initial number of species, and the rates of various events allowed to happen in the system (birth, mutation, migration, immigration) and the parameters that control the shape of the mortality-function (the carrying capacity of lattice sites, the death rate

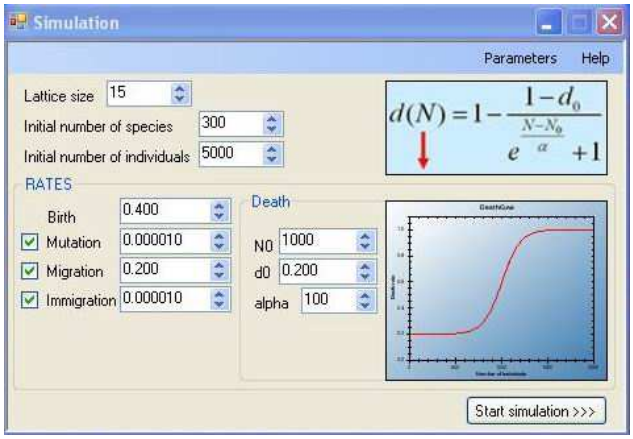

Figure 2. Screenshot of the *Simulation* application

for the case of a single individual on a lattice site, the variable that controls the steepness of the function). The modification of the default parameter values can be performed through the user interface. The parameters from the last simulation (if any) can also be reloaded (*Parameters→Last simulation* menu option). Whenever the modifications affect the parameters of the mortality-function, the death-rate curve gets replotted for the new parameter values.

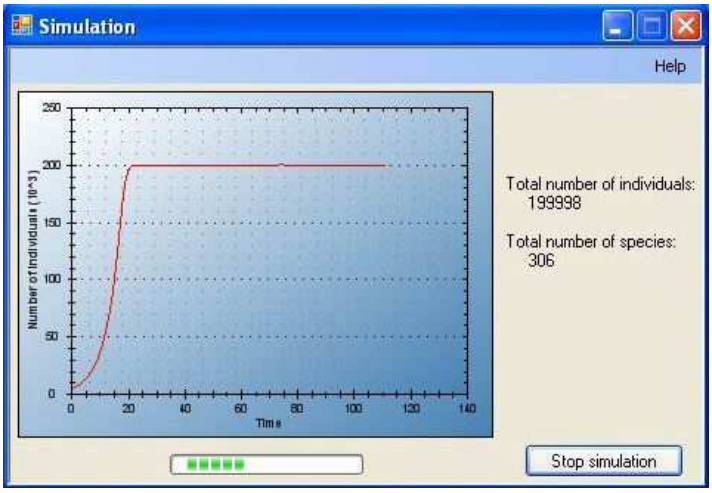

Figure 3. Screenshot of the application during simulation

The simulation can be suspended any time by clicking the *Stop simulation* button. At this point the user has three choices: to get back to the main window and specify another set of parameters for a new simulation (*Back* button), to let the suspended simulation going on (*Continue* button), to definitively interrupt the suspended simulation and exit the application (*Exit* button). In the latter case, the output files with all relevant data of the simulation are created. These data files can be analyzed using the application specially developed to complete this task.

Data analysis: This application uses the output files created by the *Simulation* to reconstruct the state of the lattice in the final simulation moment. All the significant graphs and maps respecting the statistical patterns of species distribution, abundance and diversity can be easily produced by the built-in options of this program. Figure 4 presents a screenshot of the application. The lattice itself is visualized, facilitating to select rectangular regions of the lattice (selected cells are painted blue), thereby separating local communities inside the whole metacommunity, and investigating the characteristics of these specified regions.

By default, the application seeks for data files in the directory of its executable. If they can be found in the same directory, the corresponding lattice is displayed and one can apply the built-in functionalities of the program. Otherwise the user has to specify the access path to the data files (*Data Files* menu option).

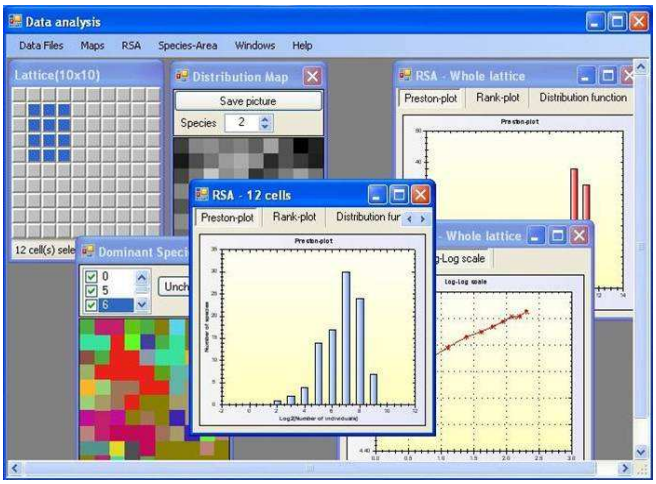

Figure 4. Screenshot of the *Data Analysis* application

All the program actions can be activated through the menu-bar and keyboard shortcuts. The items of the menu-bar and its drop-down menus are presented below:

Maps→Distribution map: This option visualizes the spatial distribution of a given species. Species are denoted by numbers in order of their abundance (species-number), 0 stands for the most abundant species. In a separate window, the cells of the lattice are painted with shades of gray ranging from white to black, according to the number of individuals that belong to the considered species. The darker the cell, the higher the number of individuals it contains of a given species. By default, the distribution of the most abundant species is presented. Other species' distribution can also be visualized by specifying its species-number in the edit box located above the lattice. The distribution map of a given species can be saved as a bmp image for further use (*Save picture* button).

Maps→Dominant species: This option identifies the dominant species in each lattice site and visualizes their distribution on the lattice. A random color is assigned to each species that turned out to be dominant in at least one lattice site. The cells are painted with the color of their dominant species. Whether the spatial distribution of a dominant species is visualized or not, depends on the status of the check box beside its species-number in the list box located above the lattice. By default, the spatial arrangement of all dominant species is visualized.

RSA: This option creates the generally used plots for representing the species-abundances distribution (Preston-plot, rank-abundance plot, and the distribution function) and presents them on separate tabbed panes of the RSA- window:

Preston-plot tab: The species abundance distribution histogram is constructed by considering abundances intervals increasing as a power of 2 and counting the number of species with sizes found within these intervals.

Rank-plot tab: The rank-abundance graph is created by sorting the individual number of each species in descending order, and plotting their proportion to the total number of individuals against the species rank.

Distribution function tab: The distribution function is created in the same way as the Preston-plot, but in this case the number of species in each interval is divided by the length of the interval and total number of species in the system.

The graphs characterizing the species abundances distribution can be constructed for the whole lattice (*RSA→Whole Lattice*) or only for the selected cells (*RSA→Selected Area*).

Species-Area: The species-area curve is constructed by calculating the average number of different species found in square regions of the lattice as the size of the area increases. The species-area curve is presented both on linear and log-log scale. As in the case of the *RSA* menu option, the species-area scaling can be calculated for the whole lattice (*Species-Area→Whole lattice*) or only for the specified region (*Species-Area→Selected area*).

Correlation: Considering a species with N individuals and denoting by $N_{i,j}$ the number of individuals belonging to this species at the site (i, j), the autocorrelation function for a distance *r* relative to this site is defined as:

$$C_{i,j}^{r} = \frac{\sum_{\substack{m,n \\ dist[(i,j)\to(m.n)]=r}} \left(N_{i,j} - \langle N \rangle\right)\left(N_{m,n} - \langle N \rangle\right)}{n_r \left(\langle N^2 \rangle - \langle N \rangle^2\right)} \qquad (2.)$$

In the above formula the summation is defined for all sites that are at distance *r* from the selected (i, j) site and n_r denotes the number of such sites. The total autocorrelation function for a distance r is calculated as:

$$C(r) = \frac{\sum_{i,j} C_{i,j}^{r}}{k_r} \qquad (3.)$$

where k_r represents the number of cells that has at least one neighboring cell at r distance.

By default, this menu option creates the autocorrelation function of the most abundant species considering the whole lattice (*Correlation→Whole*

lattice) or the specified region (*Correlation→Selected area*). The unit of the horizontal axis on the linear scale is one lattice cell size. The autocorrelation function characterizing other species' spatial distribution can also be visualized by specifying its species-number.

Simulation results

We have performed extended computer simulations on the presented complex model by using our Neutral Community Simulator Software. We present here results that reproduce in many aspects well the experimental results obtained from the BCI data set.

The considered lattice had a size of 20×20 cells, initialized with 5000 individuals belonging to 350 different species. The carrying capacity of the lattice sites was specified to be $N_0 = 1000$ individuals. This value with $d_0 = 0.2$ and $\alpha = 50$ parameter values, resulted a rather sharp slope of the death-rate curve. The other parameters used in the simulations were set as follows: $b = 0.4$, $m = 0.00001$, $q = 0.1$ and $w = 0.00001$. Inside the lattice, a square of 14×14 lattice sites was selected as a local community for statistical study.

On Figure 5. RSA is constructed as the probability density function of finding a species with a given abundance. Simulation results (Figure 5.a) exhibit good agreement with the BCI experimental data (Figure 5.b): the exponent of the power-low fit is -0.89 for simulation data, while in case of the BCI data this exponents take values around -1.

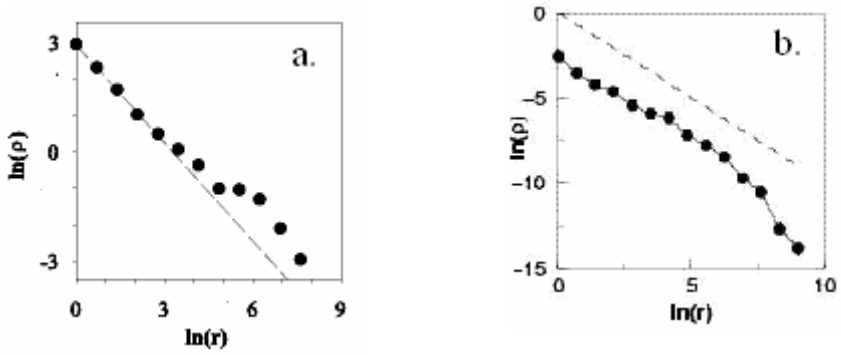

Figure 5. Relative Species Abundances as the probability density function of finding a species with a given abundance. On figure **a** dots are from computer simulations and the dashed line indicates a power-low fit with exponent -0.89. Figure **b** presents this probability density function for the Barro Colorado tropical forest tree census. The dashed line on figure **b** illustrates the power-low with exponent -1.

The Preston-type representation of RSA is presented on Figure 6 both for the simulation data (Figure 6.a) and the BCI data set (Figure 6.b).

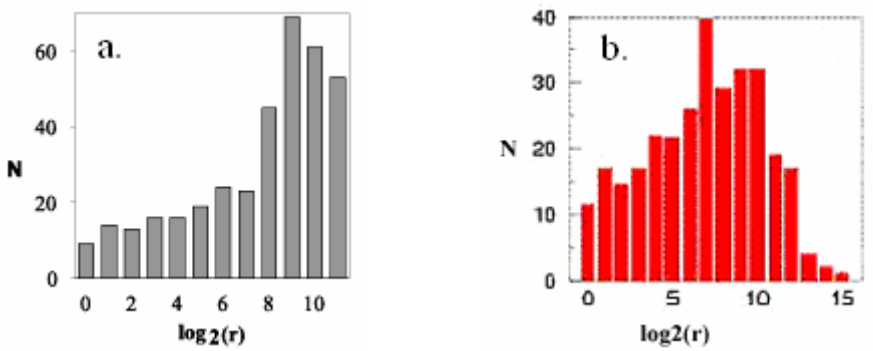

Figure 6. Relative Species Abundances in Preston-type representation. Figure **a** is constructed from simulation data, figure **b** illustrates RSA for the Barro Colorado tropical forest tree census.

On Figure 7. species-area curves are constructed. Each point on these curves represents the average number of species in quadrates of the same size of the simulation grid (Figure 7.a) and the 50 ha BCI tropical forest respectively (Figure 7.b). The species-area curve, constructed from simulation data, has a scaling behavior with exponent 0.37. For the 1990 year's BCI data this curve follows a power-low with exponent 0.23.

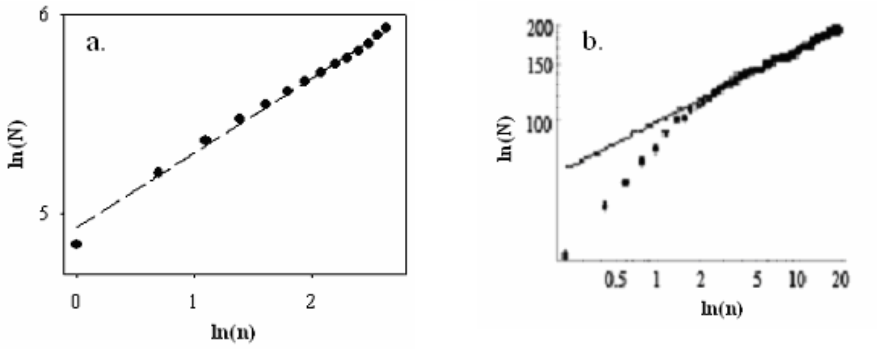

Figure 7. Species-Area scaling. On figure **a** dots are simulation results and the dashed line indicates a power-low fit with exponent 0.37. Figure **b** presents the species-area scaling for the BCI tropical forest tree census for year 1990. The best fit for experimental data resulted a power-low with exponent 0.23. Unit of horizontal axes: one lattice cell size (figure **a**), 1 ha (figure **b**)

Computer simulations resulted autocorrelation functions with exponentially decreasing initial part, followed by values fluctuating around 0. This behavior of the autocorrelation function characterizes each species, independently of their abundance. On Figure 7.a the initial part of the autocorrelation function of species with various abundances is presented. However, experimental data exhibits power-low behavior of the autocorrelation function for abundant species (Figure 8.b).

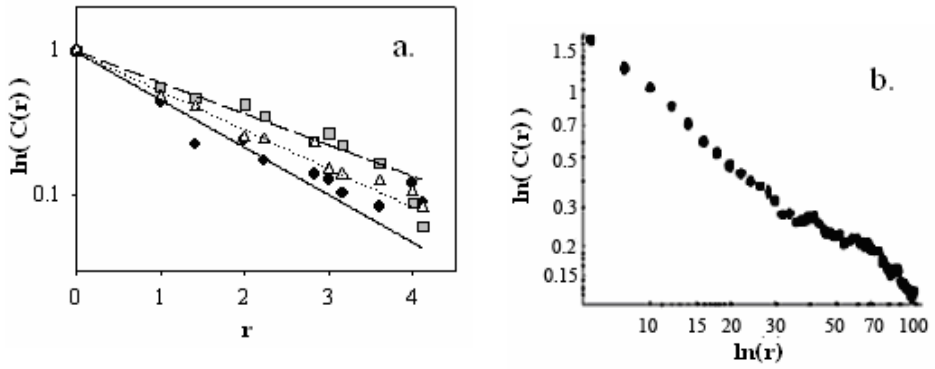

Figure 8. The autocorrelation functions and exponential fits for species with various abundances are presented on figure **a**. Figure **b** illustrates the power-low behavior of the autocorrelation function of the most abundant species in the BCI data set.

Conclusions

We have introduced here a complex spatially extended neutral model along with the related simulation software. Computer simulations on this model resulted in quite good power-low exponents both for the species abundances distribution and species-area scaling. The -0.89 exponent of the power-low fit for the probability density function approximates well the values obtained from experimental results in case of the BCI tree data set. The 0.37 exponent of the species-area scaling is in the $[0.2-0.5]$ exponents-interval characteristic of the BCI data. However, the autocorrelation function resulted from computer simulations doesn't confirm the trend from the experimental data: the former resulted exponential decay while the latter exhibits power-low behavior.

The obtained results show improvements relative to the mean-field like previous models, reproducing in the same time both the observed RSA

and species-area scaling. The fact that we fail to reproduce the good trend for the species autocorrelation function suggests that this model need also further improvements.

Acknowledgements

The present study was supported by a Word Federations of Scientist National Scholarship.

REFERENCES

1. Hubbel, S.P. *The Unified Neutral Theory of Biodiversity and Biogeography*. - Princeton Univ.Press, Princeton, New Jersey (2001).
2. Hubbel, S.P. *Tree Dispersion, Abundance, and Diversity in a Tropical Dry Forest* - Science 203: 1299-1309 (1979).
3. MacArthur, R. H. and Wilson, E. O. *The Theory of Island Biogeography* - Princeton, N.J.: Princeton University Press (1967)
4. Bell, G. *Neutral Macroecology*. - Science 293: 2413-2418 (2001).
5. Norris, S. *Neutral Theory, a New, Unified Model of Ecology*. - BioScience 53: 124-129 (2003).
6. Chave, J. *Neutral theory and community ecology*. - Ecology Letters 7: 241-253 (2004).
7. Chave, J., Muller-Landau H.C. and Levine S.A. 2002. *Comparing classical community models: theoretical Consequences for Patterns of Diversity*. - The American Naturalist 159: 1-23.
8. Preston, F.W. *The canonical distribution of commonness and rarity.* Part I and II. - Ecology 43: (185–215), 410–432 (1962).
9. Derzsi, A., Horvát, Sz., Néda, Z. 2006. *Studies of neutral macroecological models* – resumé
10. Derzsi. A, Néda, Z. 2006. *Neutral Community Simulator Software* URL:http://atom.ubbcluj.ro/~aderzsi/neutral.html

STUDIA UNIVERSITATIS BABEŞ-BOLYAI, PHYSICA, LII, 2, 2007

TRANSPORT PHENOMENA AND AC-SUSCEPTIBILITY OF (Bi;Pb):2223 SUPERCONDUCTORS DOPED WITH Sm IONS

M. BODEA[*], P. BALINT[*], T. R. YANG[**], A.V. POP[*], C. LUNG[*], G. ILONCA[*]

ABSTRACT. The effect of partial substitution of Ca by Sm on the structural, transport and magnetic properties of $(Bi_{1.6}Pb_{0.4})Sr_2(Ca_{1-x}Sm_x)_2Cu_3O_y$ superconductors ceramics ($0 \leq x \leq 0.015$) have been investigated. The substitution of Sm at the Ca site induced the decrease of the volume fraction for the 2223 phase and the increase of 2212 and 2201 phase volume fractions. The nature of T_c suppression may be attributed to the increase of oxygen content in Bi_2O_2 double layers with increasing Sm concentrations. The samples shows a linear dependence of intergranular temperature as a function of AC field amplitude, which is in agreement with Muller critical state model.

1. Introduction

The substitution of an 4f element, such Sm, for Ca in Bi:2223 and Bi:2212, can indirectly affect the processes from CuO_2 layers due to the influence it has on the large transfer from BiO layers to CuO_2 layers [1,2].

In the Bi:2212 phase, the reduction of the BiO valency (less than 3+) reveals that the BiO layers acts as hole reservoirs [3]. The carrier concentration is one of the most crucial parameters which determine the critical transition temperature T_c.

Substitution studies at the Ca site by Sm^{3+} ions in Bi:2212 superconductor causes a repulsion between the CuO_2 layers thereby increasing the CuO_2 - CuO_2 plan separation. The increase in Sm concentration, induce the increase of excess oxygen incorporated between the Bi_2O_2 double layers [4,5]. Moreover, the mechanism that governs the T_c suppression as well as the mechanism of conduction at higher doping levels has not reported, hitherto.

[*] Babes-Bolyai University, Faculty of Physics, Str. M. Kogalniceanu no. 1, 400084, Cluj – Napoca, Romania.

[**] National Taiwan Normal University, Department of Physics, No. 88 Sec 4, Thingchou Rd, Taipei 117, Taiwan, ROC.

Substitution studies by Sm at the Ca site in (Bi,Pb):2223 superconductor are very few in the literature.

In order to obtain more information, we are interested in changes in the electronic states due to the substitution of Sm ions into Ca sites of (Bi,Pb):2223 compounds.

2. Experimental

The samples with nominal composition $(Bi_{1.6}Pb_{0.4})Sr_2(Ca_{1-x}Sm_x)_2Cu_3O_y$ (x=0.00-0.025) were synthesized by conventional solid-state reaction [6]. Appropriate amounts of high purity oxides and carbonates were thoroughly mixed and ground for 3h. The mixed powder was subjected to a four – steps calcinations treatment each of 20h in air with intermediate grinding and pressing between steps. The first step was performed at 800℃. Subsequent steps were performed at temperature up to 850℃ in flowing oxygen. The samples were examined by X-ray diffraction (XRD) and energy dispersive X-ray analysis (EDAX). The electrical resistivity was measured by standard four probe DC method using a Keithly 220 programmable current source and the Keithley 2182 sensitive digital voltmeter. The contacts were made with silver paste and golden leads were attached to the specimens.

Cylindrical specimens were cut from sintered samples and used for AC-susceptibility using a Lake Shore Model 7000 AC susceptometer.

The measurements were performed at a frequency of 666.7 Hz as a function of temperature at fixed AC magnetic field amplitude (H_{ac}) in a range from 2 at 100 Am^{-1}.

3. Results and discussions

The XRD analysis confirmed the presence of a single Bi-2223 phase in x = 0.00 samples [7]. Figure 1 shows the XRD patterns of x = 0.00, x = 0.015 Sm samples. The XRD analysis on the samples with x = 0.025 Sm have confirmed a multiphase structure.

The peaks of the XRD-patterns (002) and (008, as well as 2223 (002) and (0010) and others peaks, were marked with 2 and 3 respectively for comparison of the phases 2212 and 2223.

Most of the identified peaks belong to the Bi-2223 and Bi-2212 phases with a few low intensity peaks belonging to the Bi-2201 phase. The volume fraction of the Bi-2223 phase was estimated as in Ref. [8,9] by using the XRD peak intensity of (0010) in Bi-2223 and the (008) peak intensity in Bi-2212 phase decreases to 55, 60 and 50% for x=0.015 Sm. A gradual change of Bi-2223 phase into Bi-2212 was evidenced with increasing Sm concentration a results also obtained for Er. [8].

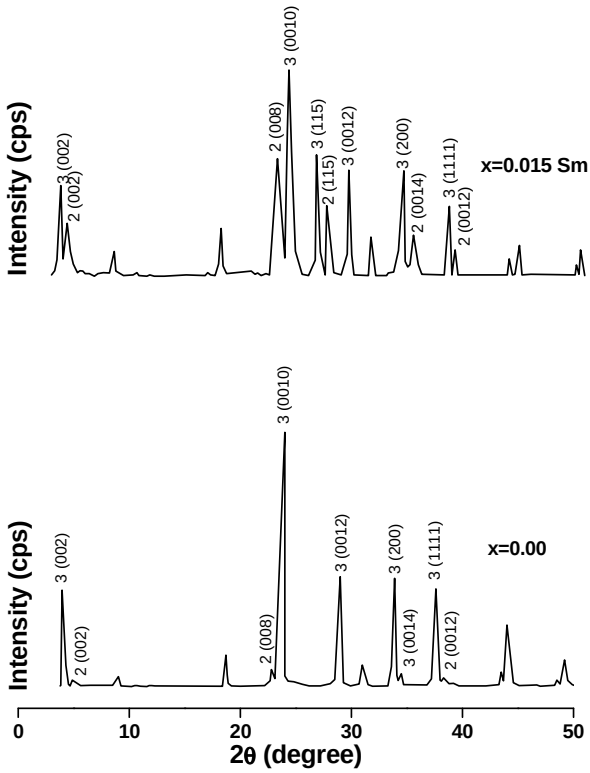

Figure 1. The X-ray diffraction patterns of $(Bi_{1.6}Pb_{0.4})Sr_2(Ca_{1-x}Sm_x)_2Cu_3O_y$ samples

The temperature dependence of the resistivity for all samples in the normal state are characterized by formula $\rho_n = \rho_0 + aT$ in the temperature range 110-300K, which can be see in figure 2. By using the temperature dependence of the resistivity the residual resistivities $\rho(0)$ the critical temperature T_c, and the width temperature transition ΔT_c were determined (Table 1).

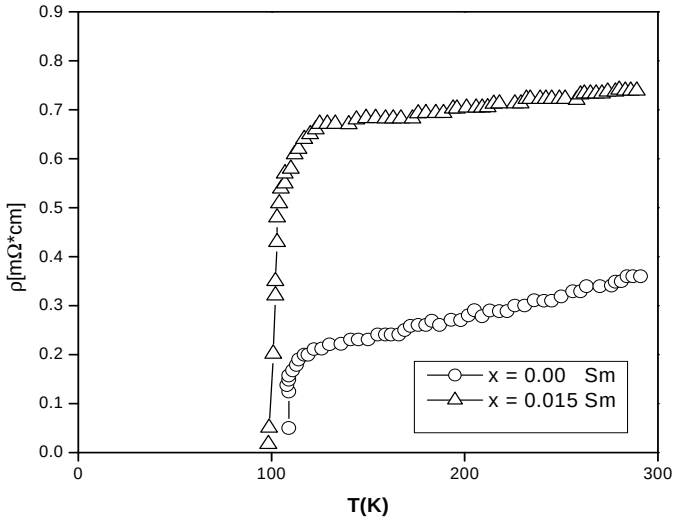

Figure 2. Temperature dependence of the electrical resistivity in the $(Bi_{1.6}Pb_{0.4})Sr_2(Ca_{1-x}Sm_x)_2Cu_3O_y$ samples

For the sample with x=0.015 the residual resistivity increases compared with the x=0.00 sample, showed in Table 1. The increase in residual resistivity in the sample with x = 0.015 may be connected by the mixed 2223-2212 phases and the reduction of charge carrier in the CuO_2 plan.

Table 1.

Resistivity parameters and the crystalline phase content in x=0.00 and x=0.015 Sm samples.

Samples	T_c (K)	ΔT_c (K)	$T_c(\rho = 0)$ (K)	$\rho(0)$ $(\mu\Omega \cdot cm)$	Phase content		
					2223	2212	2201
x=0.00	108	4.2	106.0	95	94%	6%	-
x=0.015	102.00	7.0	98.0	830	58%	32%	7%

The rate of suppression from T_c is around 4K/at% for x=0.015 Sm. This results agrees with the supposition that the magnetic moment of Sm^{3+} play a minor role in the mechanism of T_c suppression.

Figure 3 shows the real part $\chi'(T)$ and imaginary part $\chi''(T)$ of the complex susceptibility behavior for different AC fields for x = 0.015 Sm samples. $\chi'(T)$ decreases below T_c and saturates at low temperatures. The

temperature and field dependence of $\chi'(T)$ and $\chi''(T)$ shows a two stage behavior which is found to be typical for sintered HTS. For the x = 0.015 samples, $\chi''(T)$ exhibits a single peak centered at T_p.

The intergranular peak centered at T_p shifts considerably to lower temperature at x = 0.0015 for Sm samples when AC-field amplitude is increased. For the x = 0.00 samples the imaginer part of the AC-susceptibility, $\chi''(T)$, exhibit two peaks at T_p for intergranular transition and T_g for intragranular transition respectively. Our x = 0.015 Sm samples exhibits a single peaks at T_p. The absence of intergrain peak in $\chi''(T)$ suggests the presence of smaller decoupled grains in x = 0.015 Sm samples [10].

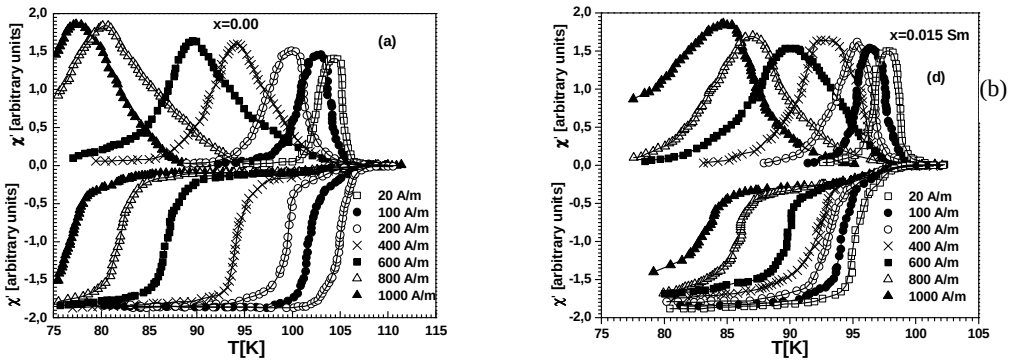

Figure 3. Temperature dependence of the real part χ' of the AC susceptibility and the imaginary part χ'' for $(Bi_{1.6}Pb_{0.4})Sr_2(Ca_{1-x}Sm_x)_2Cu_3O_y$ where x is: (a) x=0.00, (b) x=0.015 Sm.

In our samples the critical transition temperatures, T_{cg} [the end of superconductor diamagnetism for $\chi'(T)$] are very close to the inflection point temperature T_c in the resistivity measurements and T_p values are nearly the same as the zero resistivity temperatures $T_c(\rho = 0)$ [11], as shown in Table 2.

In order to investigate the effect for partial substitution with Sm^{3+} on intergranular pinning force, we studied the T_p as a function of H_{ac} for x = 0.00 and x = 0.015 Sm samples shown in figure 4. The T_p versus H_{ac} is described by formula

$$T_p = T_{po} - A \cdot H_{ac}$$

in agreement with Muller critical state model [12].

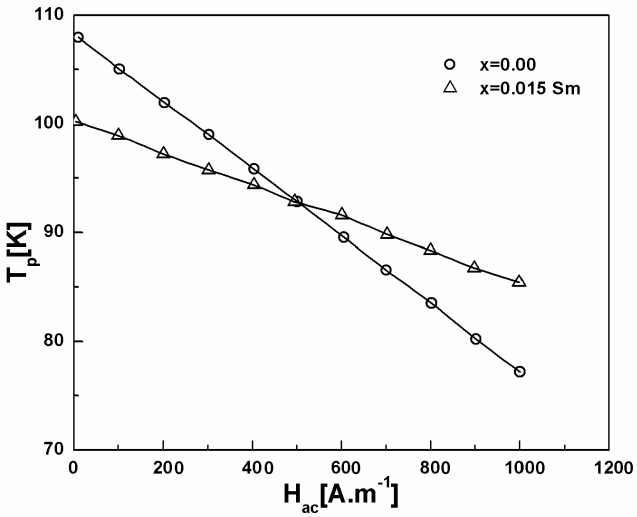

Figure 4. Intragranular χ`` - peak temperature versus ac-field amplitude for Bi:2223 doped with x = 0.00 Sm and x = 0.015 Sm samples.

Table 2.

AC – susceptibility parameters in x=0.00 and x=0.015 Sm samples.

Samples	T_c (K)	ρ_0 $(\mu\Omega \cdot cm)$	T_p (K)
x=0.00	108	95	106.6
x=0.015 Sm	102	830	98.5

4. Conclusions

Substitutions by x = 0.015 Sm in the Ca site of the (Bi,Pb):2223 superconductor induced additional 2212 and 2201 phases. The temperature dependence of the electrical resistivity is about linear in the normal state. The residual resistivity varies as a function of the content of Sm, $T_c(\rho = 0)$, the transition width ΔT_c and the transition T_c are a dependence of the content of substituting ions of Sm. The magnetic nature of the substitute up x = 0.015 Sm does not play an important role in the mechanism of T_c

suppression in (Bi,Pb):2223 superconductor. The samples show a linear dependence of the intergranular temperature as a function of ac field amplitude, which is in agreement with the Muller critical state model [12].

REFERENCES

1. K. Watanabe, Supercond. Sci. Technol. 11 (1998) 843;
2. G. Ilonca et. al. Int. J. Inorg. Mat. 3 (2001) 769;
3. R. Ramesh, B. G. Bagley, J. M. Tarascon, S. M. Green, M. L. Rudee and H. L. Luo, J. Appl. Phys. 67 (1990) 379;
4. Y. Gao, P. Permabuco-Wise, J. E. Crow, J. O'Reilly, M. Spencer, H. Chen and R. E. Solomon, Phys. Rev. B 45, (1992) 7436;
5. P. Sumana Prabhu, M. S. Ramahandra Rao, U. V. Varadaraju and G. V. Subba Rao, Phys. Rev. B 50, (1994) 6929;
6. A. V. Pop, G. Ilonca, D. Ciurchea, M. Ye, I. I. Geru, V. G. Kantser, V. Pop, M. Todica, R. Deltour, J. Alloys Compounds 24 (1996) 116;
7. A. V. Pop, R. Deltour, A. Harabor, D. Ciurchea, G. Ilonca, V. Pop, M. Todica, Supercond. Sci. Technol.10 (1997) 843;
8. K. Nanda Kishore, S. Satyavathi, V. Hari Babu, O. Penea, Mater. Sci. Eng. B 38 (1996) 267;
9. Y. S. Sung, H. Kumakura, K. Togano, Physica C 331 (2000) 171;
10. K. Kupfer, I. Apfelsted, R. Flukinger, C. Keller, R. Meiner-Hirmer, Runtsch, A. Turowski, U. Wiech, T. Wolf, Cryogenics 29 (1998) 268;
11. A. V. Pop, G. Ilonca, D. Ciurchea, M. Ye, R. Deltour, I. I. Geru, Int. J. Mod. Phys. B. 10 (1996) 967;
12. H. Muller, Physica C 159 (1988) 717.

STUDIA UNIVERSITATIS BABEŞ-BOLYAI, PHYSICA, LII, 2, 2007

MICROWAVE ABSORPTION IN CHROMOSOMAL DNA MOLECULES

CRISTINA M. MUNTEAN[*], ANDREI IOACHIM[**], DUMITRU MOLDOVEANU[***]

ABSTRACT. An open problem in the important research field on the low-frequency dynamics of DNA double helix is related to the direct absorption of microwave energy in DNA polymers.

In this work, microwave characteristics of insertion loss and return loss have been measured between 7.3-12.4 GHz, for aqueous solutions of chromosomal and total DNA and for the corresponding buffer, respectively. Starting with the physics analysis of insertion loss and return loss, we have calculated the relative electric-field attenuation constants and the percentage of the incident microwave power attributed from this data analysis to the absorption in DNA-hydration layer systems. The method used is applicable to calculation of microwave absorption in substances that form hydration layers with water.

A broadband influence of low-intensity microwaves is reported here for all the molecular systems investigated by us, over the entire frequency range.

Keywords: dissolved DNA, microwave absorption, electric-field attenuation constant, low intensity microwaves

INTRODUCTION

The direct absorption of moderate-to-low-frequency nonionizing electromagnetic radiation in DNA molecules, is a potential source of biological effects [1,2] including the influence of nonthermal microwave power, at selective frequencies, on replication and transcription processes. These phenomena might be important with regard to the identification of

[*] National Institute for Research-Development of Isotopic and Molecular Technologies, R-400293 Cluj-Napoca, P. O. 5, Box 700, Romania
To whom correspondence should be addressed. Telephone: +40-264-584037; Telefax: +40-264-420042; e-mail: cmuntean@s3.itim-cj.ro
[**] National Institute of Materials Physics, P. O. Box MG-7, R-76900 Bucharest-Măgurele, Romania
[***] Institute of Developmental Biology, Bucharest 77748, Splaiul Independenței 296, Romania

cellular targets during the resonant interactions of complex systems with a microwave field. Particularly, such a system could be a higher-order structure of DNA molecule [1,2].

A variety of microwave measurements of aqueous solutions of DNA have been reported, with a number of different results [3-13]. There are several factors which might be responsable for this diversity of experimental evidence. Among them, the limited frequency range over which the measurements have been made and the variety of the samples used, have been mentioned [10, 13].

The microwave absorption signature of dissolved DNA permits the identification of the direct absorption of microwave energy in the biopolymer and in the hydration layer, respectively. As an introduction to the study of this phenomenon, we have carried out at GHz-frequencies (7.3-12.4 GHz), basic microwave measurements of insertion loss and return loss [12-14]. Besides, we have calculated in this frequency range the relative electric-field attenuation constants and the percentage of the incident microwave power absorbed in dissolved DNA molecules.

The aim of this paper is to report some of our data on microwave absorption of different DNA-hydration layer systems, as reflected by scalar microwave measurements of insertion loss and return loss.

MATERIALS AND METHODS

DNA samples

We have investigated several chromosomal and total DNA samples, extracted by standard techniques from different types of bacterial cells cultures. Samples were isolated and purified in our laboratories. After each extraction, DNA molecules were dissolved in a storage buffer (10 mM Tris-HCl, 1 mM EDTA, pH = 8) and the sample quality was checked by UV spectrophotometric method. For this purpose a Specord UV-VIS with a pair of tandem cells was used. Agarose gel electrophoresis with standard markers has also been used in some cases. Our samples were nonuniform ones, including molecular fragments of a statistic length distribution.

Microwave experiments

Basic scalar microwave measurements of insertion loss and return loss were carried out, at room temperature, with a Hewlett Packard 8755 Network Analyzer. Low-intensity microwaves (TE10 mode), at a level of the incident power of 25 mW, were used. A teflon cylindrical sample holder ($V=0.558\ cm^3$) was placed in the X-band waveguide, in a configuration of weak electric field. An impedance bridge was used to monitor the power reflected from the sample. The combined mismatches of the sample holder

with and without test samples were considered small, with less than 1% of the incident power being reflected in almost all the experimental frequency range (7.3-12.4 GHz). For a given sample, microwave characteristics of insertion loss and return loss were taken simultaneously. A signal mediated over 16 scans was considered. A schematic diagram of the experimental microwave system used in these experiments is presented in Fig. 1 [14].

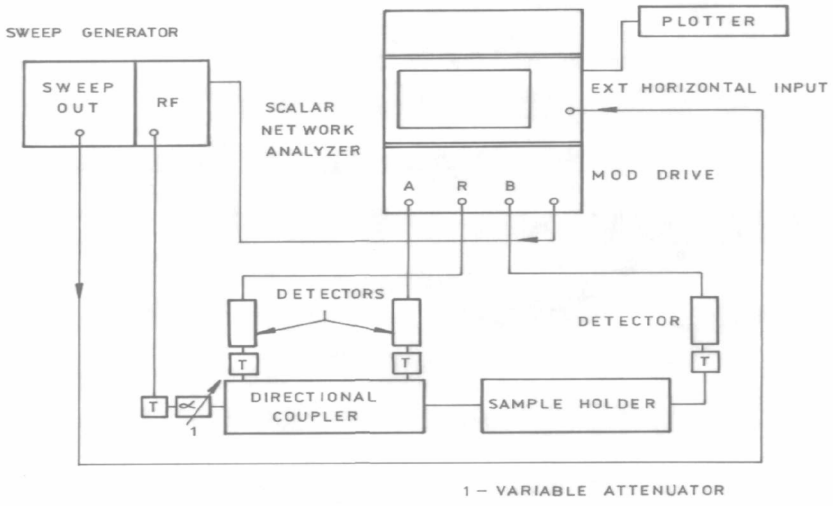

Fig. 1. Schematic diagram of the experimental microwave system.

Calculation of the absorption and attenuation parameters

The microwave response of a given aqueous solution of DNA was compared to the microwave response of the standard storage buffer, respectively, considered for the same volume. On the basis of the physics analysis of the measured quantities of insertion loss and return loss, we have estimated for each DNA sample the relative electric-field attenuation constants [13] and the ratio $\Delta P_{abs} / P_i$ (%). Here ΔP_{abs} is the difference between the power absorbed in DNA solution, $P_{DNA\ solution}$, and that in free buffer, P_{buffer}. P_i is the incident power, which was the same for the compared samples. $P_{DNA\ solution}$ includes the total microwave power absorbed in the three component volumes - solute volume, hydration layer volume and free solvent volume [10, 13]. Hence, ΔP_{abs} is the microwave power absorbed in DNA-hydration layer system.

The relative attenuation constants were estimated for each sample in two distinct ways, our data reflecting the differences which might appear in the reported values of the attenuation parameter, because of the definition used for it by the investigators or due to the measurement method and not to the sample itself. No significant differences have been found in the values of these parameters.

A preliminary communication on the evaluation of microwave absorption in DNA-hydration layer systems has already been made by us [13]. The aim of this communication was to describe the algorithm developed by us for calculating the relative electric-field attenuation constants and the percentage of the incident microwave power absorbed from this data analysis in dissolved DNA. For the calculation of the attenuation and absorption parameters we have used a computing algorithm written in Basic language, developed in our laboratories.

RESULTS

In this work, microwave characteristics of insertion loss and return loss have been measured between 7.3-12.4 GHz, for aqueous solutions of chromosomal and total DNA and for the corresponding buffer, respectively. Besides, the relative electric-field attenuation constants and the percentage of the incident microwave power absorbed in dissolved DNA molecules have been calculated in the same frequency range, starting with the physics analysis of the measured quantities of insertion loss and return loss [12-15].

Scalar microwave characteristics of insertion loss and return loss are presented in Fig. 2 for a solution of total DNA from Alcaligenes sp. (1.23 mg/ml) (_____). For comparison in the same figure the microwave characteristics of the standard storage buffer (- - - -) are given. The frequency-dependence of the insertion loss for six different chromosomal and total DNA samples (DNA_1-DNA_6) are presented in Fig. 3.

The frequency-dependence of the percentage of the incident microwave power attributable from our data analysis to the absorption in DNA-hydration layer systems are shown in Figs. 4-5, for several distinct chromosomal or total DNAs, isolated and purified in our laboratories. Besides, the frequency-dependence of the relative electric-field attenuation constants for three chromosomal DNA samples (DNA_1, DNA_3 and DNA_5) dissolved in standard storage buffer are presented in Fig. 6.

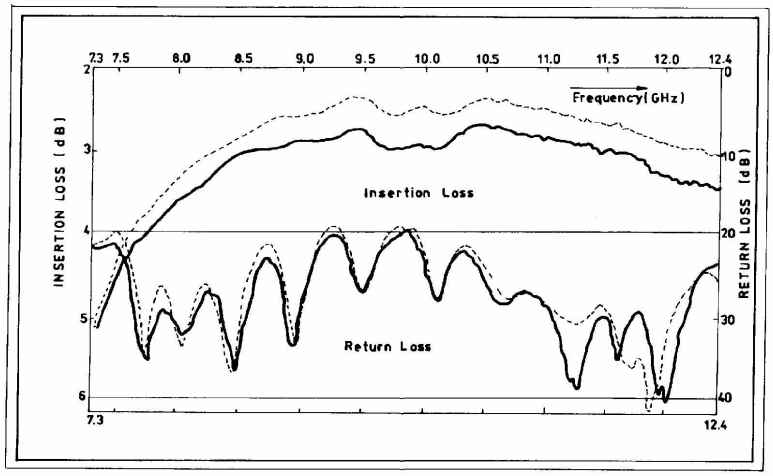

Fig. 2. The frequency-dependence of the scalar microwave characteristics of insertion loss and return loss for a solution of total DNA from Alcaligenes sp. (1.23 mg/ml) (_____). For comparison, the scalar microwave characteristics of the standard storage buffer (- - - -) are given.

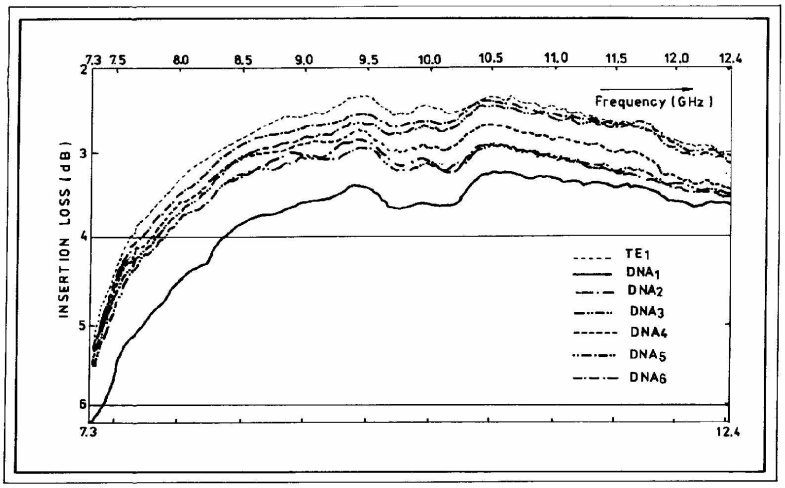

Fig. 3. The frequency-dependence of the insertion loss for six different chromosomal and total DNA samples (DNA_1-DNA_6). For comparison the insertion loss of the standard storage buffer (TE_1) is given. DNA samples are: 1) chromosomal DNA from B. megatherium (0.245 mg/ml) (DNA_1); 2) chromosomal DNA from Bacillus vulgatus (0.152 mg/ml) (DNA_2); 3) chromosomal DNA from Bacillus cereus (0.0675 mg/ml) (DNA_3); 4) total DNA from Alcaligenes sp. (1.23 mg/ml) (DNA_4); 5) total DNA from Methylomonas sp. (1.24 mg/ml) (DNA_5); 6) chromosomal DNA from λ-phage (0.962 mg/ml) (DNA_6).

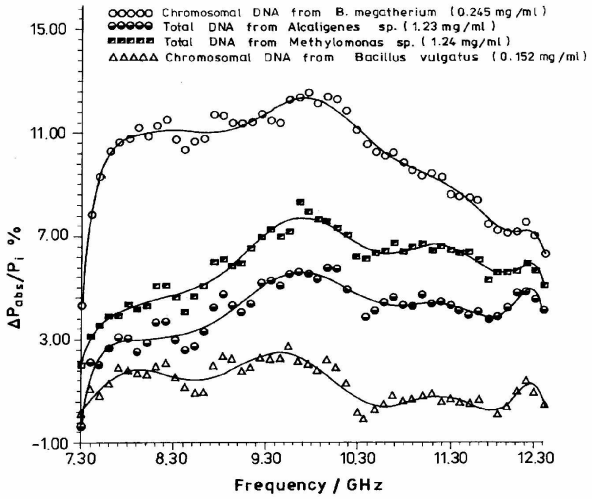

Fig. 4. The frequency-dependence of the percentage of the incident microwave power absorbed in different DNA-hydration layer systems: chromosomal DNA from B. megatherium (0.245 mg/ml) (DNA_1); chromosomal DNA from Bacillus vulgatus (0.152 mg/ml) (DNA_2); total DNA from Alcaligenes sp. (1.23 mg/ml) (DNA_4); total DNA from Methylomonas sp. (1.24 mg/ml) (DNA_5). DNA was dissolved in a standard storage buffer (10 mM Tris-HCl, 1 mM EDTA, pH = 8). A fitting routine based on a polynomial has been used.

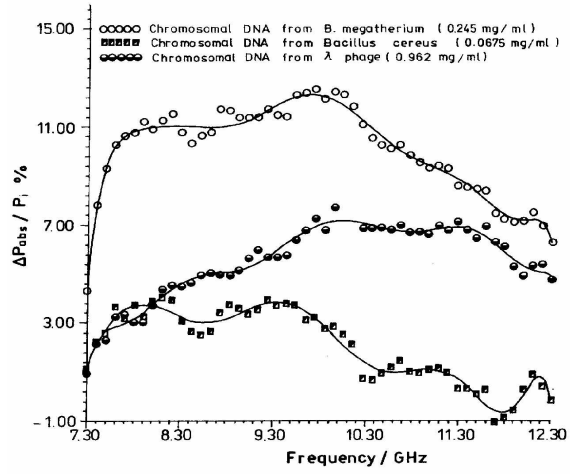

Fig. 5. The frequency-dependence of the the percentage of the incident microwave power absorbed in different DNA-hydration layer systems: chromosomal DNA from B. megatherium (0.245 mg/ml) (DNA_1); chromosomal DNA from Bacillus cereus (0.0675 mg/ml) (DNA_3); chromosomal DNA from λ-phage (0.962 mg/ml) (DNA_6). DNA was dissolved in a standard storage buffer (10 mM Tris-HCl, 1 mM EDTA, pH = 8). The microwave absorption of chromosomal DNA from B. megatherium (0.245 mg/ml) is presented for comparison. A fitting routine based on a polynomial has been used.

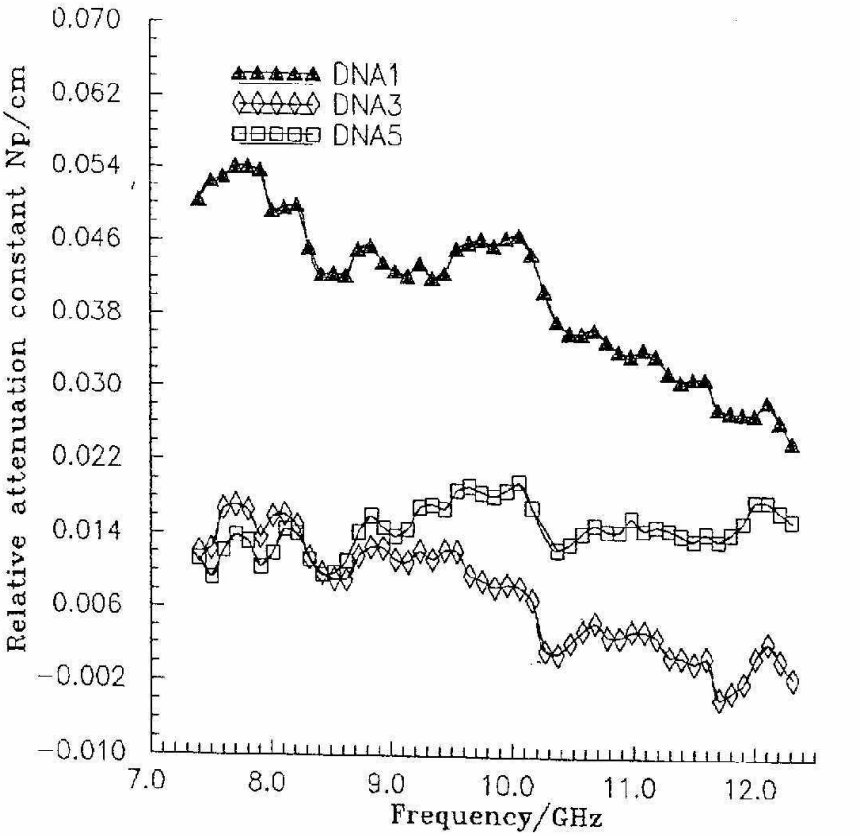

Fig. 6. The frequency-dependence of the relative electric-field attenuation constants for three DNA samples dissolved in standard storage buffer (10 mM Tris-HCl, 1 mM EDTA, pH = 8).

DISCUSSION AND CONCLUSIONS

The aim of this paper is to report some of our data on microwave absorption of different DNA-hydration layer systems, as reflected by scalar microwave measurements of insertion loss and return loss.

In this study we analyse samples containing double helical DNA, water molecules and ions. Our systems are inhomogeneous ones, being characterized by large dipole fluctuations of their molecular groups. These components are modestly polar bases, less polar sugars, negatively charged phosphates and water molecules [14-16].

The microwave absorption of certain water soluble biopolymers (DNA, proteins) in solution is composed of three parts: absorption in free water, absorption in the substance and absorption in the hydration layer [10, 13]. The Debye model of the dielectric constants, which could explain the data is presented in detail in ref. 10.

Starting with the physics analysis of the scalar microwave characteristics of insertion loss and return loss, we have calculated the relative electric-field attenuation constants and the percentage of the incident microwave power attributed from this data analysis to DNA-hydration layer systems. A direct absorption of microwave energy in the DNA-hydration layer has been found. Our study reports a broadband influence of low-intensity microwaves for all the molecular systems investigated by us, over the entire frequency range. Most of our DNA-hydration layer systems were found to absorb few percent of the incident microwave power, in the frequency range 8-12 GHz. We didn't observe for these types of samples any sharp feature which might prove the participation of acoustic modes in DNA dynamics [3,5,6].

In the following, we will present in short results obtained by other groups on the same subject. In a paper published in 1984 [3] and in the following works published in 1985 [5] and in 1986 [6], Edwards and his co-workers reported the presence of narrow band features in the 1-10 GHz microwave absorption spectrum of plasmid DNA in aqueous solution [11]. These results allowed the authors to explain the experimental observation by the existence of vibrational modes of DNA. Resonant microwave absorptions of DNA molecules were explained by the presence of internal acoustic modes of the molecules [6]. The narrow bands had longer relaxation times ($\approx$ 300 ps) than would otherwise be expected for a large molecule in intimate contact with a room temperature solvent [11]. Besides, theoretical work has suggested, that elastic coupling rather than the expected viscous coupling of the molecule to the surrounding solvent, leads to an enhancement of the lifetimes of the molecule's conventional linear normal modes [11]. Another theoretical work on microwave response of DNA in solution was presented in detail by Davis and VanZandt [17]. Their results showed that the hydration layer binding is the single most important aspect of this phenomenon. Besides, the theoretical work of Fisun and Katanaev described the resonant microwave absorption of cloned linear DNA molecules in aqueous solution [18].

However, additional experimental work performed by independent groups, failed to reproduce the observations of Edwards and co-workers [8-11]. Also, Davis, Edwards, Swicord, Sagripanti and Saffer observed no resonant absorption for long-chain DNA dissolved in saline buffer.[6]. In the paper of Gabriel and co-workers it is concluded that except for broadband

absorption due to the ionic conductivity of the DNA buffer solution, no difference existed between the samples' absorption spectrum and a reference sample of pure water[8, 11].

In the paper published by Garner, Ohkawa, Tuason, and Lee [10], based on the study of microwave absorption in substances that form hydration layers with water, in the frequency range 2-26.5 GHz, an analysis of the measured data shows that a simple Debye relaxation model of the hydration layer (which consists of ordered or 'irrotational' water moleculers) can explain the data, that this ordering of the water increases the relaxation time in the hydration layer. By fitting the absorption curve to a Debye model it was possible for these authors to calculate hydration-layer thicknesses. In general, this appears to be less than or approximately one water molecule thick. [10]. The presence of a hydration layer around DNA molecule is in agreement with other experimental observations [10].

The group of Bigio, Gosnell, Mukherjee and Saffer [11] has measured the absolute absorption spectrum of plasmid DNA (pUC8.c2), in buffered aqueous solution, between 5 and 20 GHz. They observed no absorption resonances in this frequency range, but they do see broadband differences, between DNA and pure buffer, that are attributable to changes in the ionic conductivity of the solutions [11].

In this paper we present results on DNA extracted from six different microorganisms. This fills a gap in the data in the literature, as far as chromosomal DNA is concerned. Among the absorption spectra of our samples are enough high differences which can not be explained considering the differences in concentrations. In fact, at 8.7 GHz, chromosomal DNA from ? phage absorbs only half as much as chromosomal DNA from B. megatherium, even though the solution of chromosomal DNA from ? phage is 4 times more concentrated than the second one. Besides, at 8.5 GHz total DNA from Methylomonas absorbs only half as much as chromosomal DNA from B. megatherium, even though the solution of total DNA from Methylomonas is 5 times more concentrated than the second one. Taking into account total DNA from Methylomonas (1.24 mg/ml), total DNA from Alcaligenes (1.23 mg/ml) and chromosomal DNA from ? phage (0.962 mg/ml), no such drastic differences are to be observed. In Ref. 10 it is emphasized that the Debye relaxation model predicts a linear dependence in the microwave absorption for a fixed microwave frequency as a function of solute concentration, at low concentrations. However in the above reference, data were considered for the same type of DNA (calf thymus DNA, Sigma D-1501). Considering different DNA sources as in our data, the average molecular size of the samples is different from sample to sample and there is a dependence of the broadband absorption on this parameter, as presented in Refs. 5 and 11. So in our case, polymer

concentration is not the only sample parameter to be taken into account. This suggests that the observed variability is also due to the state of the DNA molecule. This opinion is also expressed in Ref. 5.

Besides, we want to emphasize that in the literature different biopolymer concentrations were used in the microwave absorption studies. For instance, in DNA experiments from ref. 10 a concentration of 50 mg/ml was used in comparison with maximum of 1.24 mg/ml used in the present paper. For the purposes of the studies presented in Ref. 11 a polymer concentration of 0.7 mg/ml was used, which is the same concentration as in Refs. 3, 5 and 6. In Refs. 5 and 6 *E. coli* DNA concentrations were less than 0.7 mg/ml. In Ref. 9 the plasmid (puC8.c2) concentration ranged from 0.5 to 1.5 mg/ml (determined by UV absorbance).

Both in Ref. 10 and Ref. 11 a possible explanation for the broadband absorption is considered to be the contribution of the DNA solution conductivity. For example, in Ref. 10 some arguments are presented in order to sustain the argument that the conductivity contribution is not sufficient to explain the results. Microwave absorption of solutions containing electrolytes varies inversely with frequency over the range considered (2-26,5 GHz) [10]. As would be expected from the change in ionic conductivity, significant broadband changes are to be seen that are most pronounced at the lowest frequencies [11]. This is not the case for data presented by us in Figs. 4 and 5.

In conclusion, our present data, characterizing different DNA-hydration layer systems, offer information about dielectric relaxation processes at GHz frequencies [10]. Chromosomal and total DNA molecules were investigated. A broadband influence of low-intensity microwaves is reported here for all the molecular systems investigated by us, over the entire frequency range. On the basis of the Debye model of the dielectric constants, it would be possible in the future to calculate the hydration layer thickness and its relaxation time [10, 13] [1].

[1] **Acknowledgements**

The authors wish to thank to Mr. O. Petrean for writing the computing algorithm of the absorption and attenuation parameters and to Mrs. Dorica Vintila for help in sample preparation. We acknowledge fruitful discussions on microwave measurements with Dr. Gabriela Nicoara from the National Institute of Materials Physics, Bucharest-Magurele, Romania.

REFERENCES

1. Koschnitzke, C., Kremer, F., Santo, L., Quick, P., and Poglitsch, A.: A Non-Thermal Effect of Millimeter Wave Radiation on the Puffing of Giant Chromosomes, Z. Natur forsch. *38 c* : 883-886, 1983.
2. Belyaev, I.Ya., Alipov, D., and Shcheglov, V.S.: Chromosome DNA as a Target of Resonant Interaction Between Escherichia Coli Cells and Low-Intensity Millimeter Waves, Electro- and Magnetobiology *11*: 97-108, 1992.
3. Edwards, G.S., Davis, C.C., Saffer, J.D., and Swicord, M.L.: Resonant Microwave Absorption of Selected DNA Molecules, Phys. Rev. Lett. *53*: 1284-1287, 1984.
4. Edwards, G.S., Lindsay, M., and Prohofsky, E.W.: Comment on Resonant Microwave Absorption of Selected DNA Molecules and Observation of Low-Lying Raman Bands in DNA by Tandem Interferometry, Phys. Rev. Lett. *54*: 607, 1985.
5. Edwards, G.S., Davis, C.C., Saffer, J.D., and Swicord, M.L.: Microwave-Field-Driven Acoustic Modes in DNA, Biophys. J. *47*: 799-807, 1985.
6. Davis, C.C., Edwards, G.S., Swicord, M.L., Sagripanti, J., and Saffer, J.: Direct Excitation of Internal Modes of DNA by Microwaves, Bioelectrochem. Bioenergetics, *16*: 63-76, 1986.
7. Sagripanti, J.L., and Swicord, M.L.: DNA Structural Changes Caused by Microwave Radiation, Int. Radiat. Biol. *50*: 47-50, 1986.
8. Gabriel, C., Grant, E.H., Tata, R., Brown, P.R., Gestblom, B., and Noreland, E.: Microwave Absorption in Aqueous Solutions of DNA, Nature *328*: 145-146, 1987.
9. Foster, K.R., Epstein, B.R., and Gealt, M.A.: 'Resonances' in the Dielectric Absorption of DNA, Biophys. J. *52*: 421-425, 1987.
10. Garner, H.R., Ohkawa, T., Tuason, O., and Lee, R.L.: Microwave Absorption in Substances that Form Hydration Layers with Water, Phys. Rev. A *42*: 7264-7270, 1990.
11. Bigio, I.J., Gosnell, T.R., Mukherjee, P., and Saffer, J.D.: Microwave Absorption Spectroscopy of DNA, Biopolymers *33*: 147-150, 1993.
12. Muntean, C., Ioachim, A., and Cornea, C.: Microwave Absorption in Plasmidic DNA Molecules, in **Fifth International Conference on the Spectroscopy of Biological Molecules Proc**., T. Theophanides, Jane Anastassopoulou, N. Fotopoulos (eds.), Kluwer Academic Publishers, Dordrecht, the Netherlands, 71-72, 1993.
13. Muntean, C., Ioachim, A., and Petrean, O.: Evaluation of Microwave Absorption in DNA-Hydration Layer Systems, in **6th European Conference on the Spectroscopy of Biological Molecules Proc**., J.C. Merlin, S. Turrell, J. P. Huvenne (eds.), Kluwer Academic Publishers, Dordrecht, the Netherlands, 333-334, 1995.

14. Muntean, C.M., Banciu, G., Cozar, O., and Ioachim, A.: Microwave Response of DNA Polymers with Counterion Distribution, in **Spectroscopy of Biological Molecules: New Directions**, J. Greve, G. J. Puppels, C. Otto (eds.), Kluwer Academic Publishers, Dordrecht, the Netherlands, 223-224, 1999.
15. Muntean, C.M., Cozar, O., Banciu, G., and Pop, S.: Microwave Absorption Spectroscopy of DNA Polymers in the Presence of Cu(II) Ions, Proc. Suppl. Balkan Phys. Lett. *5*: 211-214, 1997.
16. Yang, L., Weerasinghe, S., Smith, P.E., and Pettitt, B.M.: Dielectric Response of Triplex DNA in Ionic Solution from Simulations, Biophys. J. *69*: 1519-1527, 1995.
17. Davis, M.E., and VanZandt, L.L.: Microwave Response of DNA in Solution: Theory, Phys. Rev. A *37*: 888-901, 1988.
18. Fisun, O.I., and Katanaev, M.O.: Theoretical Study of Resonant Microwave Absorption by DNA in Aqueous Solution, Makromol. Chem. *192*: 1191-2202, 1991.
19. Edwards, G., Ying, G., and Tribble, J.: Role of Counterions in the Gigahertz Relaxation of Wet DNA, Phys. Rev. A *45*: R8344-R8347, 1992.

STUDIA UNIVERSITATIS BABEŞ-BOLYAI, PHYSICA, LII, 2, 2007

TIGHT-BINDING MOLECULAR DYNAMICS SIMULATIONS OF RADIATION INDUCED FRAGMENTATION OF C_{60}

LÓRÁND HORVÁTH[*], TITUS A. BEU[**]

ABSTRACT. The fragmentation of C_{60} fullerene was investigated using tight-binding molecular dynamics simulations based on the parameterization of Papaconstantopoulos et al. 1. By averaging the fragment size distributions obtained from random sets of initial configurations, the radiation induced fragmentation in the 50-500 eV excitation energy range was studied. For high excitation energies, predominantly multifragmentation occurs and a power-law dependence of the small fragments is observed. For low excitation energies, the fragment size distributions are peaked at values higher than 1. A phase transition is found in the 100-120 eV energy range. The results are compared with experimental time of flight fragment size distributions and are in good agreement with similar studies.

Keywords: fullerene, fragmentation, tight-binding, molecular dynamics

1. Introduction

The fragmentation of fullerene ions induced in collisions with atomic and molecular targets has been widely studied since macroscopic amounts of fullerenes were first made available. The detection of fragments resulting from experiments dealing with the collision of a target by different projectiles is usually performed with time-of-flight (TOF) spectrometers 6,8,9. The first systematic study of fullerene fragmentation was done by O'Brien et al. using ns laser pulses 2. The primary channel of photodissociation was found to be the loss of neutral C_2 or C_3 units.

Energetic, vibrational and electronic properties of large carbon nanostructures (such as fullerene polymers or carbon nanotubes) using *ab initio* / DFT calculations are not effective on many up-to-date computers. This is the reason for which there is an obvious need for alternative methods, involving less computational effort, but preserving the level of accuracy achieved by DFT methods.

[*] University "Babeş-Bolyai", Faculty of Physics, M. Kogălniceanu 1, 400084 Cluj-Napoca, Romania

[**] University "Babeş-Bolyai", Faculty of Physics, M. Kogălniceanu 1, 400084 Cluj-Napoca, Romania, E-mail: tbeu@phys.ubbcluj.ro

A valuable alternative is the tight-binding (TB) approach, extensively applied in our previous work for the study of covalent systems 3,4,5. The tight-binding total-energy (TBTE) models can be viewed as simplified two-center-oriented *ab initio* methods, where the properties of the system can be calculated from a parameterized representation of the Kohn-Sham equation, in the Roothaan-type matrix form 11,12.

The TB parameterization employed in our study is the scheme proposed by Papaconstantopoulos et al. 1, which accurately describes the relative energies of several different structural phases, the elastic constants of the ground state phase and the occupied electronic bond structure relative to first-principle methods. The parameterization was also shown to very accurately describe the structure and the vibrational properties of C_{60} and C_{70} fullerenes, and of C_{36} oligomers 3,4,5.

Collision-induced dissociation is a powerful technique to investigate the fullerene fragmentation process (electrically neutral or charged) 10. The impact with various projectiles (photons, electrons, atoms or molecules, ions or other fullerenes) reveal the fact that the fragmentation can occur via different channels depending on the projectile type and its impact energy 6:

$$\begin{aligned} C_{60}^{r+} &\rightarrow C_{60-2n}^{r+} + C_{2n}^{0} \\ C_{60}^{r+} &\rightarrow C_{60-m}^{(r-k)+} + C_{m}^{k+} \\ C_{60}^{r+} &\rightarrow \sum_{m,k} C_{m}^{k+} \end{aligned} \qquad (1.1)$$

where the possible processes are: (a) evaporation of light neutral even numbered C_{2n}^{0} clusters, (b) asymmetric dissociation (fission) into heavy and light (neutral or charged) fragments, m<<60, and (c) multifragmentation into several light fragments.

2. Non-orthogonal tight-binding molecular dynamics (TBMD)

In tight-binding total-energy models the total energy of the system can be expressed as a sum over the occupied one-electron energies (eigenvalues of the Kohn-Sham equations) and a short-range repulsive pair potential

$$E_{tot}(\{\vec{R}_J\}) = \sum_{k=1}^{n_{occ}} n_k \boldsymbol{\mathcal{E}}_k(\{\vec{R}_J\}) + \sum_{J<K} V_{rep}(|\vec{R}_{JK}|). \qquad (2.1)$$

The one-electron energies $\boldsymbol{\mathcal{E}}_k$ are the eigenvalues of the Roothaan matrix representation of the Kohn-Sham equations:

$$(H - \boldsymbol{\mathcal{E}}_k S) C^k = 0, \qquad (2.2)$$

where the Hamiltonian matrix, H, and the overlap matrix, S, are expressed

relative to some non-orthogonal set of atom-centered orbitals. C^k is the eigenvector corresponding to eigenvalue ε_k.

The Kohn-Sham formalism allows the eigenvalues to be shifted by an arbitrary constant. In the employed TB scheme the eigenvalues are shifted by a structure and volume dependent constant (eliminating the pair potential), so that the total energy of a given structure is given by the sum of the shifted one-electron energies ε'_k 1

$$E_{tot}(\{\vec{R}_J\}) = \sum_{k=1}^{n_{occ}} n_k \varepsilon'_k(\{\vec{R}_J\}). \qquad (2.3)$$

By obtaining the partial derivatives for the one-electron energies from equation (2.2), the forces can be expressed analytically:

$$\vec{F}_I = -\sum_{k=1}^{n_{occ}} \frac{n_k}{C^{k+} S C^k} C^{k+} \left(\frac{\partial H}{\partial \vec{R}_I} - \varepsilon_k \frac{\partial S}{\partial \vec{R}_I}\right) C^k, \quad (2.4)$$

this being a significant advantage for large-scale MD simulations.

The bonding between adjacent carbons in a fullerene occurs on a curved surface which leads to an sp^3 bonding, the number of electrons for a molecule composed of N atoms being $n = 4N$. The occupation number for a closed-shell system is $n_k = 2$ and the number of occupied electronic states is $n_{occ} = n/2$. Having 4 valence electrons for every carbon atom, the number of atomic orbitals for the molecule is $4N$.

The $4N \times 4N$ Hamiltonian matrix for the system of the valence electrons is composed of 4×4 blocks, each block corresponding to the interaction between the s, p_x, p_y and p_z orbitals of the pair of atoms involved

$$H = \begin{bmatrix} \ddots & \vdots & & & \vdots & & \vdots & & & \vdots & \\ \cdots & h_s^I & 0 & 0 & 0 & \cdots & H_{ss}^{IJ} & H_{sx}^{IJ} & H_{sy}^{IJ} & H_{sz}^{IJ} & \cdots \\ & 0 & h_p^I & 0 & 0 & & -H_{sx}^{IJ} & H_{xx}^{IJ} & H_{xy}^{IJ} & H_{xz}^{IJ} & \\ & 0 & 0 & h_p^I & 0 & & -H_{sy}^{IJ} & H_{xy}^{IJ} & H_{yy}^{IJ} & H_{yz}^{IJ} & \\ \cdots & 0 & 0 & 0 & h_p^I & \cdots & -H_{sz}^{IJ} & H_{xz}^{IJ} & H_{yz}^{IJ} & H_{zz}^{IJ} & \cdots \\ & \vdots & & & \vdots & \ddots & \vdots & & & \vdots & \end{bmatrix}. \qquad (2.5)$$

The diagonal on-site Hamiltonian matrix elements, h_λ^I are expressed in terms of the local pseudo-atomic density, ρ_I. The elements of the non-diagonal blocks of the Hamiltonian matrix, $H_{\lambda\lambda'}^{IJ}$, have the Slater-Koster form 7 and they are obtained from the two-center hopping parameters $H_{ss\sigma}^{IJ}, H_{sp\sigma}^{IJ}, H_{pp\sigma}^{IJ}, H_{pp\pi}^{IJ}$ using the bond direction cosines $\gamma_x^{IJ}, \gamma_y^{IJ}, \gamma_z^{IJ}$. The overlap matrix, S, has a similar form to the Hamiltonian, excepting the unitary diagonal blocks.

The diagonal on-site Hamiltonian elements depend on the local pseudo-atomic density ρ_I in terms of a Birch-like equation:

$$h_\lambda^I = \alpha_\lambda + \beta_\lambda \rho_I^{2/3} + \gamma_\lambda \rho_I^{4/3} + \chi_\lambda \rho_I^2, \qquad (2.6)$$

where λ = s, p.

The elements of the non-diagonal blocks of the Hamiltonian are parameterized as polynomials, multiplied by an exponential cutoff function

$$\begin{aligned} H_{\lambda\lambda'\mu} &= (a_{\lambda\lambda'\mu} + b_{\lambda\lambda'\mu} R + c_{\lambda\lambda'\mu} R^2)\, e^{-d_{\lambda\lambda'\mu}^2 R}\, f(R), \\ S_{\lambda\lambda'\mu} &= (\delta_{\lambda\lambda'} + p_{\lambda\lambda'\mu} R + q_{\lambda\lambda'\mu} R^2 + r_{\lambda\lambda'\mu} R^3)\, e^{-s_{\lambda\lambda'\mu}^2 R}\, f(R). \end{aligned} \qquad (2.7)$$

The employed parameterization defines a pseudo-atomic density for each atom as a sum of exponential contributions given by the atoms in the environment:

$$\rho_I = \sum_{J \neq I}^{N} e^{-\lambda^2 R_{IJ}}\, f(R_{IJ}). \qquad (2.8)$$

The parameterization uses a cutoff function, which vanishes for $R > R_c$:

$$f(R) = \frac{1}{1 + \exp[(R - R_c)/\Delta]}. \qquad (2.9)$$

For carbon, $R_c = 10.5 a_0$ and $\Delta = 0.5 a_0$ values are employed, where a_0 is the Bohr radius.

In the employed TB parameterization each carbon atom has four valence electrons tightly bound to the atoms, but the ionization of the atoms is not taken into account. In spite of the fact that the covalent bonds play an explicit role in the model, the obtained fragments will always be electrically neutral. It is expected that the fragment size distribution obtained with TOF spectrometers would slightly differ from the distributions obtained with the tight-binding model because the distribution peaks in the experimental methods are summations over the total number of electrically neutral and/or charged clusters.

3. Simulation details

The starting geometry of the C_{60} fullerene used in our simulations is the one obtained from geometry optimizations carried out using simulated annealing embedded in molecular dynamics using the above mentioned TB framework 3,4. The bond lengths of the initial fullerene obtained with the TB model are 1.37 and 1.45 Å for the double and single bonds, respectively.

The radiation input was simulated by suddenly heating up the system. Specifically, this implies assigning randomly oriented velocities to the atoms, such that the total kinetic energy of the molecule amounts to the transferred excitation energy. The approximation of sudden energy transfer is appropriate because the typical fragmentation time, found to be around 0.5-2.5 ps, exceeds significantly the short fs laser pulses used in laser induced fragmentation experiments.

The excitation energy is a reference quantity appropriate for this study because we can compare our results with those obtained from experimental fragmentations using electrons or ions, where the so-called deposited energy, the equivalent of the excitation energy, can actually be measured. 8

The employed excitation energies were taken in the energy interval 50 – 500 eV. In terms of binding energy per molecule, these energies correspond to the range 0.08 E_{bind} – 0.83 E_{bind}, or to the 3200 – 32000 K temperature range.

Since the excitation energy is distributed between the translational and rotational degrees of freedom of the fragments, one would need as deposited energy roughly twice the total binding energy of the fullerene (which is approximately 600 eV) in order to fully dissociate the molecule.

Each fragmentation trajectory was propagated at constant energy until a stopping criterion was satisfied. The individual fragments were identified by a recursive labeling algorithm, which basically extends the fragments gradually by atoms lying within a given cutoff distance 4. The cutoff distance was set to 2 Å, which is approximately 50% above the average bond length of the initial C_{60} fullerene. The stopping criterion is satisfied if each atom maintains its belonging to a fragment over the last 0.25 ps, which is roughly 10% of the maximum duration considered for a trajectory.

Because of the very statistical nature of the studied process, an ensemble of 200 C_{60} molecules were fragmented for the mentioned range of excitation energies and, for each value of the energy, the profiles of the fragment size distributions were summed up and then normalized to the total number of resulted fragments. The fragment size distributions for some representative excitation energies are presented in Figure 1.

The plotted distributions show a gradual shift of the distribution maximum from large fragment sizes to smaller ones. The U-shape of the distributions at intermediate energies is also apparent. However, there are two important aspects which have to be emphasized. Firstly, the fragmentation of the fullerene occurs at excitation energies of approximately 95 eV. For energies below this value, the molecule remains stable over a very long period of time, only a slight deformation of the C_{60} cage being noticed. Secondly, for low values of the excitation energy, the fragment size

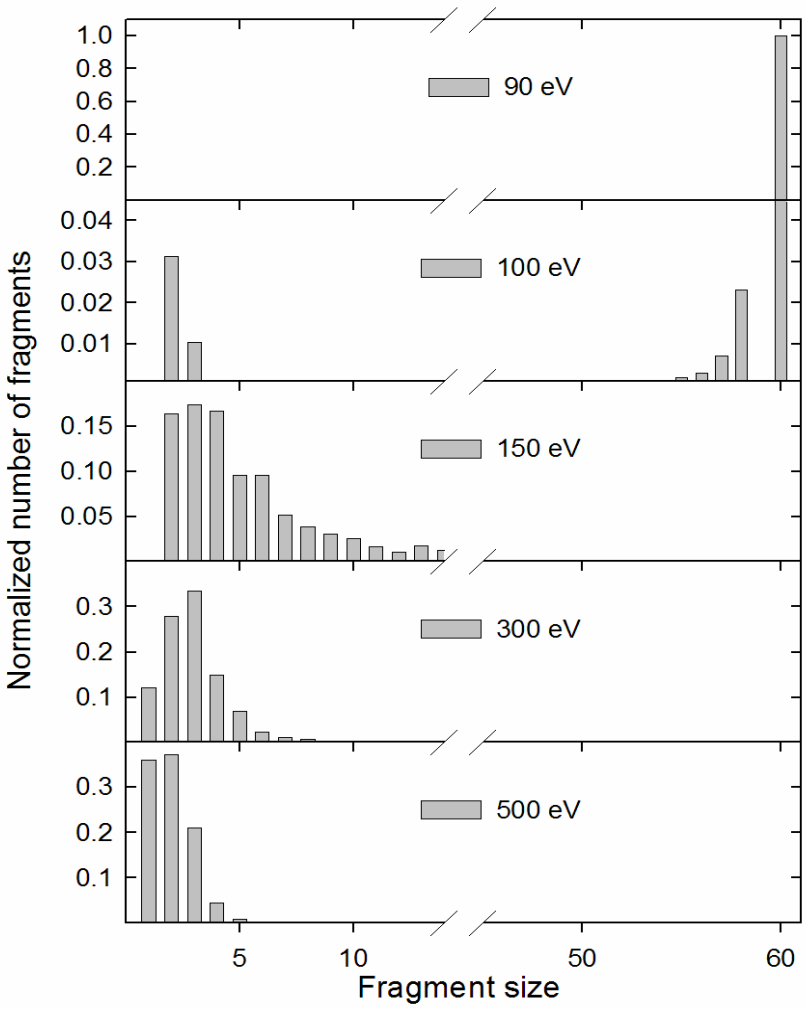

Figure 1. Normalized number of fragments for some excitation energies

distributions are not peaked at $n = 1$ (single C-atoms), but at higher values ($n = 2$ or 3). There is also another noticeable trend: the contribution of the monomers increases more rapidly with the excitation energy than those of the immediately larger sizes (dimers and trimers).

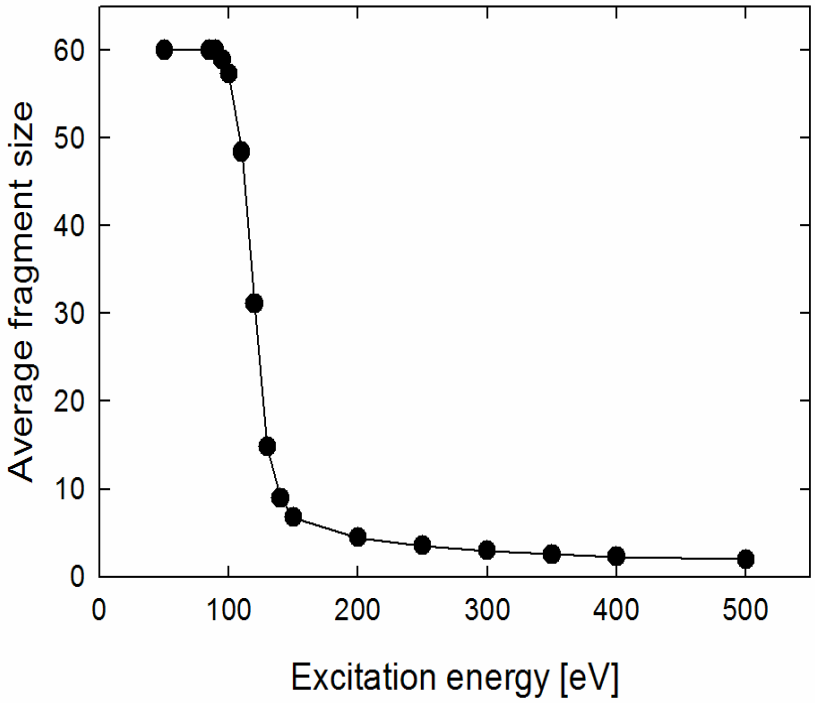

Figure 2. Average fragment size plotted against the excitation energy

For each of the excitation energies, several characteristic quantities were studied as functions of the excitation energy. The average fragment size, plotted in Figure 2, was defined as the cumulative number of atoms divided by the cumulative number of fragments.

The average minimum (maximum) fragment size, defined as the cumulative number of atoms contained in the minimum (maximum) fragments divided by the cumulative number of minimum (maximum) fragments is presented in Figure 3.

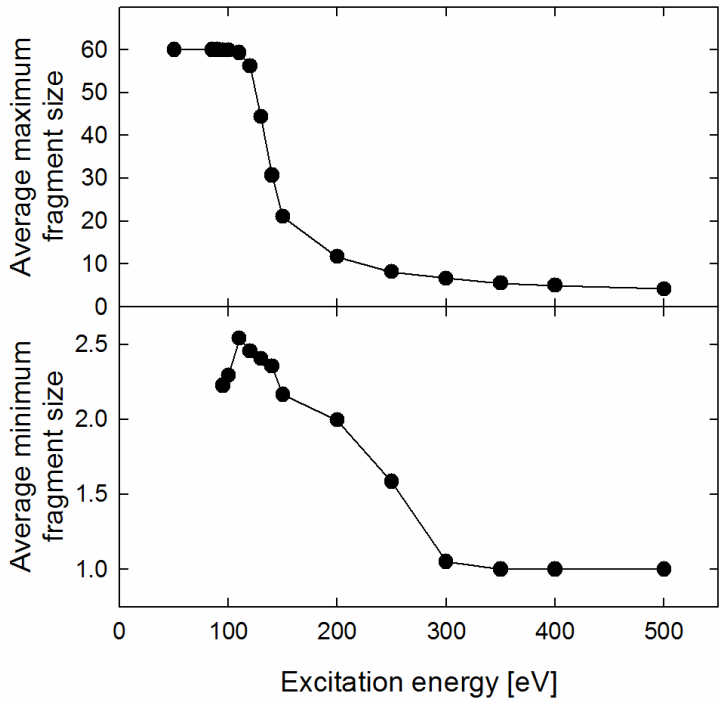

Figure 3. Average minimum and maximum fragment size plotted against the excitation energy

The average maximum fragment size behaves similarly to the average fragment size distribution. In contrast, the average minimum fragment size distribution peaks in the 100-120 eV excitation energy range. This particular energy interval is associated with a phase transition, which is apparent in each distribution yielded by our simulations. An overall minimum (maximum) fragment size was also defined as the smallest (largest) fragment in the whole trajectory ensemble and in the phase transition region its behavior is similar to the average fragment size.

The average binding energy/atom is obtained by averaging over the whole trajectory ensemble the total binding energy of the fragments for each trajectory divided by the total number of atoms. In the employed parameterization the binding energy for a carbon atom in the initial fullerene is 10.00 eV, in fairly good agreement with the value of 9.55 eV, obtained from DFT calculations using the functional PBEPBE and the 6-31G(d) basis set. The dependence of the average binding energy at the end of the trajectories

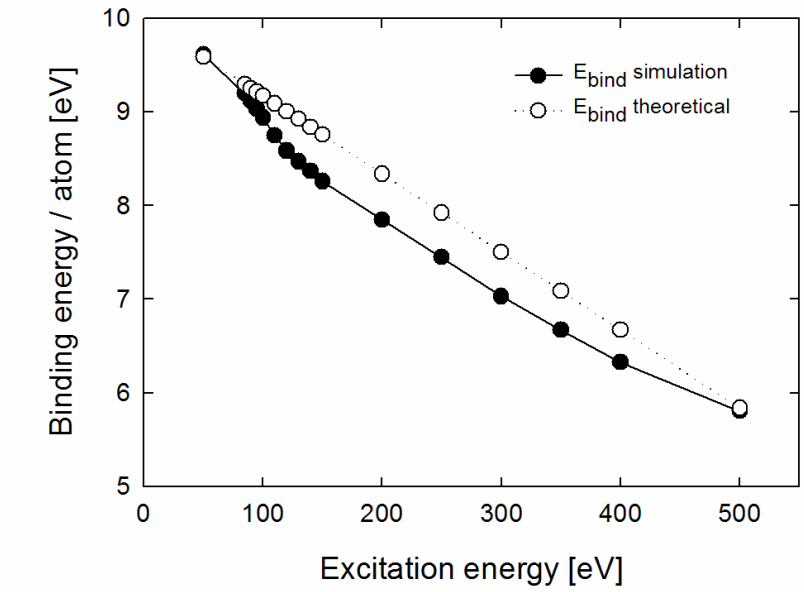

Figure 4. Simulated and theoretical binding energy vs. excitation energy

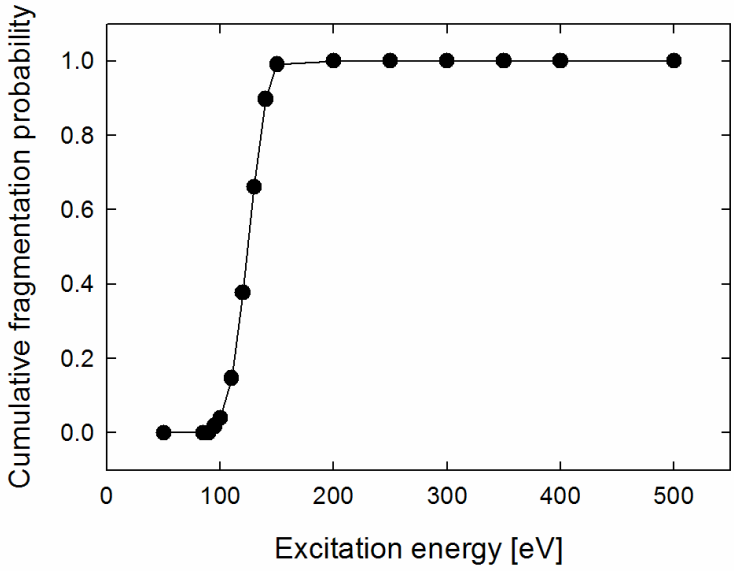

Figure 5. The cumulative fragmentation probability shows a phase transition for 100-120 eV excitation energies

on the excitation energy is compared in Fig. 4 with theoretical values. As expected, the theoretical values are linearly decreasing with the excitation energy. However, the simulations show a slight underestimation of the corresponding theoretical values. This is, probably, due to the fact that in the phase transition zone the molecule is in an excited state and the binding energy per atom becomes smaller than the theoretically predicted one.

The cumulative fragmentation probability, defined as the total number of dissociated fullerenes divided by the total number of trajectories, is depicted in Figure 5 and clearly shows the phase transition in the already mentioned energy range (100-120 eV).

4. Conclusions

The fragmentation process for the C_{60} fullerene was simulated using tight-binding molecular dynamics (TBMD) simulations based on the parameterization of Papaconstantopoulos et al. 1. The radiation-induced fragmentation process was studied in the excitation energy range 50-500 eV. For each excitation energy fragment size distributions were calculated by averaging the distributions obtained by dissociating a set of 200 fullerenes, with kinetic energies randomly assigned to the initial configurations. The overall results regarding fragment size distributions are similar to those obtained in several time-of-flight experiments 8,9,10,13. The so-called U-shape form of the distributions was confirmed.

Fragment size distributions, average fragment sizes, average minimum (maximum) fragment sizes, binding energies and cumulative fragmentation probabilities were calculated for each excitation energy.

For the small fragment sizes and excitation energies above 400 eV a power-law dependence of the size distribution is obtained. Multifragmentation was found to be the main fragmentation channel, but for lower energies, evaporation of small clusters plays an important role.

For low excitation energies the distribution of small fragments are not peaked at the monomer, but rather at higher fragment sizes (dimer or trimer). Fragments with high even number of atoms (over 50) are more likely to occur than odd size fragments, the primary fragmentation channel being the sequential loss of neutral C_2 units. The loss of C_3 units was found to be another fragmentation channel, but only in the intermediate energy range (300-400 eV).

In the 100-120 eV energy range a phase transition was found, in fairly good agreement with the results of the above mentioned experiments and in similar tight-binding molecular dynamics simulations 14.

REFERENCES

1. D.A. Papaconstantopoulos, M.J. Mehl, S.C. Erwin, and M.R. Pederson, Math. Res. Soc. Symp. Proc. 491, 221 (1998).
2. S.C. O'Brien, J.R. Heat, R.F. Curl, and R.E. Smalley, J. Chem. Phys. 88, 220 (1988).
3. T.A. Beu, J. Onoe, and K. Takeuchi, Eur. Phys. J. D 10, 391 (2000).
4. T.A. Beu, J. Onoe, and K. Takeuchi, Eur. Phys. J. D 17, 205-212 (2001).
5. T.A. Beu, J. Onoe, and A. Hida, Phys. Rev. B 72, 155416 (2005).
6. V.V. Afrosimov, A.A. Basalaev, M.N. Panov, O.V. Smirnov, Fullerenes, Nanotubes, and Carbon Nanostructures 12, 485 (2004).
7. J.C. Slater, G.F. Koster, Phys. Rev. 94, 1498 (1954).
8. Rentenier, P. Moretto-Capelle, D. Bordenave-Montesquieu, and A. Bordenave-Montesquieu, J. Phys. B 38, 789-806 (2005).
9. D.M. Gruen, Nucl. Instrum. Meth. B 78, 118 (1993).
10. E.B. Campbell, F. Rohmund, Fullerene reactions Rep. Prog. Phys. 63, 1061 (2000).
11. W.A. Harrison, Solid State Theory, 1970.
12. W.A. Harrison, Electronic Structure and the Properties of Solids, 1980.
13. Th. Frauenheim, G. Seifert, M. Elstner, Phys. Stat. Sol 217, 41 (2000).
14. C.Z. Wang, C.H. Xu, C.T. Chan, and K.M. Ho, J. Phys. Chem. 96, 3563 (1992).

STUDIA UNIVERSITATIS BABEŞ-BOLYAI, PHYSICA, LII, 2, 2007

SPECTROSCOPIC AND ELECTRIC SIGNAL MEASUREMENTS OF THE RETINAL RECONSTITUTED BACTERIORHODOPSIN

KLÁRA MAGYARI[1], ZOLTÁN BÁLINT[2], VIORICA SIMON[1], GYÖRGY VÁRÓ[2]

ABSTRACT. Bacteriorhodopsin (BR) discovered in *Halobacterium salinarium* is a light-driven proton pump. The light-sensitive chromophore in the protein is a retinal bound to a lysine via a protonated Schiff base.

This study aims to describe the charge motion after the *all*-trans retinal is bound to the protein. For this purpose we compared the spectroscopic and electric signals of the reconstructed retinal deficient membrane suspension, reconstructed bleached membranes and the wild-type BR purple membranes.

The apparent pK_a for the bleached BR and retinal deficient BR shifted toward higher pH values compared to the wild-type BR. Although measured at the same pH 7, the electric signals in both retinal reconstituted samples showed a significantly higher pH characteristic, compared to the wild type. This allows concluding that the retinal binding pocket was different in the three samples.

Keywords: Retinal protein, Retinal reconstitution

1. Introduction

The retinal protein bacteriorhodopsin (BR) acts as a light-driven proton pump embedded in the purple membrane from *Halobacterium salinarium* [1-3]. In this organism, the purple membrane contains only BR in a highly oriented two-dimensional hexagonal crystalline form. The energy of a light quantum absorbed by the all-*trans* retinal, bound to Lys 216 of the protein, is used to transport a proton from the cytoplasmic to extracellular regions of the cell.

The retinal in the protein is in thermal equilibrium in two forms the all-*trans*, 15-*anti* and 13-*cis*, 15-*syn* configuration when the protein is dark-adapted. The light-adapted protein contains only all-*trans*, 15-*anti* retinal.

[1] Department of Physics, University „Babes-Bolyai" Cluj-Napoca, Romania
[2] Institute of Biophysics, Biological Research Center of the Hungarian Academy of Sciences, Szeged, H-6701, Hungary

After light excitation, both retinal conformations exhibit a photocycle, but only the all-trans retinal containing protein has proton transport activity.

The structures of bacteriorhodopsin is know with 1.55 Å resolution [4].

The transporting photocycle is formed by a succession of intermediates (noted K, L, M, N and O). Each intermediate has a well determined absorption spectrum [5] and electrogenicity [6].

After absorbing the light, a charge separation along the retinal chain occurs in the fs time domain [7], followed by an all-*trans* to 13-*cis* isomerization in several ps, reaching the state K. In K to L translation, a local rearrangement around the retinal occurs in less than 10 μs. The next step is the L to M_1 translation, about 100μs after the excitation, the transfer of the proton from the Schiff base to the proton acceptor Asp-85 and the proton is release from the release group on the surface of the membrane close to the external medium [8]. In BR, refinement of the sequential model has led to introduction of 'silent' intermediates. These are specially indistinguishable substates that differ from one another in some properties of the protein. The most important 'silent transition' is the M_1 to M_2 transition, when the protein switches between the extacellular and cytoplasmic conformations, after deprotonation of the Schiff base in about 100μs [9]. The Schiff-base is reprotonated by the proton donor Asp 96 on the cytoplasmic side, reflected by appearance of intermediate N, followed by the uptake of the proton from the surrounding medium. When the retinal isomerizes back to all-*trans*, the red-shifted intermediate O appears and the protein relaxes back to the initial BR state [10, 11]. At low pH, below the pK_a of the proton acceptor group, the photocycle does not translocate across the membrane and has only red shifted intermediates [12].

To measure the electric signal of light-activated protein such BR, it is important to have an electrically anisotropic sample containing oriented proteins.

Oriented samples can be obtained by incorporating BR into a bilayer lipid membrane [13, 14]. Another method for electric signal measurement is the oriented attachment of purple membranes to a lipid-impregnated filter [15] or onto a thin teflon sheet [16]. These techniques are very sensitive to the charge motion inside the protein, but having a small optical density, make the absorption kinetic measurements rather difficult.

A possibility to eliminate this problem is to apply an external electric field to the purple membrane suspension, orienting the membrane fragments by their permanent dipole moment [17, 18]. If the membranes are incorporated in acrylamide gel and an external electric field is applied during the polymerization of the gel the orientation can be fixed [18]. The disadvantage of the technique is the low rezistivity of the sample at high salt concentration.

The electric signals measured for different BR-containing oriented-purple membrane systems demonstrated a remarkably good correlation with the photocycle [17, 19]. In principle, the electric dipole moment of each intermediate will be function of the charge configuration in the protein, which depends on the positions of the amino acid side chains and the proton transported ion.

The light activated bleaching of the purple membrane in presence of hydroxylamine was observed earlier [20, 21]. In this process the retinal reacts with the hydroxylamine forming retinaloxime, which is released from the protein and can be separated from the membrane suspension. Adding back the retinal to the apomembrane suspension, obtained from hydroxylamine bleaching, or retinal deficient *Halobacterium salinarium* strain, the purple color of the membranes can be reconstituted [22, 23].

In this study the function of three type of BR was compared: the wild-type, bleached and retinal deficient bacteriorhodopsin after retinal additon.

2. Materials and methods

In the following experiments three purple colored samples were used: the unmodified purple membrane suspension (wild type BR), the hydroxylamine treated and retinal reconstructed (bleached BR) and the originally retinal deficient BR membranes.

Purple membranes were isolated from *Halobacterium halobium* strain S9 according to a standard procedure [24]. The retinal deficient BR membranes were isolated from the strain JW2N. The bleached BR membranes were obtained from wild-type BR, illuminated for 20 hour in 1 M hydroxylamine solution at pH 7, as described [25]. The bleached membranes were washed extensively by multiple centrifugations in distilled water. To the retinal deficient and bleached BR all-*trans* retinal was added [26]. By these three purple colored samples were obtained: the unmodified purple membrane suspension (wild type BR), the hydroxylamine treated and retinal reconstructed (bleached BR) and the originally retinal deficient BR membranes.

The spectral measurements were carried out on BR polymerized in acrylamide gel, following the procedure described elsewhere [27], at room temperature, using a Unicam UV/Vis spectrometer. The thoroughly washed gels were soaked overnight in 100mM NaCl, 20mM MES (2-[N-morpholino]ethanesulfonic acid), 20mM TRIS and 20mM acetic acid buffers at the desired pH.

For electric signals measurements, oriented gel samples were prepared [28]. The gels were equilibrated with a bathing solution containing 100mM NaCl and buffers, 25mM MES or 25mM TRIS.

Data were recorded, after laser excitation of the sample on the linear time scale, and converted to a logarithmic time scale. The linear-to-logarithmic conversion was accomplished by averaging the linear time point between two logarithmic time points, which improved the signal-to-ratio at later time points.

Laser excitation was with a frequency-doubled Nd-YAG laser (Surelite 10, Continuum, Santa Clara, CA), of 1.52 mJ/cm^2 energy density at 532 nm.

The electrogenicity of the intermediates was defined earlier [29] as the change in the dipole magnitude of the intermediate to the ground state.

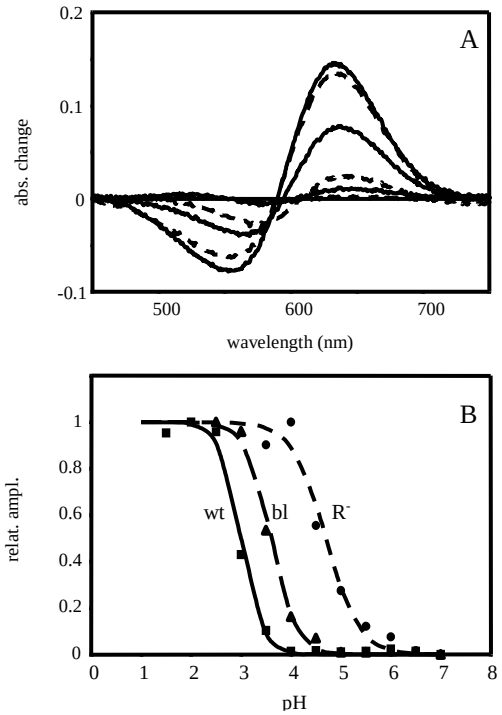

Fig. 1. The spectral titration of the wild-type, bleached and retinal deficient BR. The difference spectra of the wild-type BR. Measuring conditions: 100mM NaCl, 20 mM MES, 20 mM TRIS and 20 mM citric acid in the pH range 1.5 to 7 The difference spectra of wild-type BR (A). The relative change calculated at 560 nm and 640 nm yields titration curves for each BR (B). The apparent pK_a is 2.6 for wild-type BR, 3.6 for the bleached BR and is 4.8 for the retinal deficient BR.

The electric current signal in the measuring circuit by the change of the electrogenity is

$$i(t) = B\sum_j E_j \frac{dC_j}{dt}$$

were B is a constant determined by the electric circuit and C_j is the concentration of the *j*th intermediate. If an intermediate is missing or its concentration is constant throughout the whole photocycle, it has no electric signal. The change of the protein depends on the external condition (pH, ionic strength, etc) the electrogenicity of the intermediates could depend also on these conditions.

The electric signals arise only from the dipole magnitude changes in the direction perpendicular to the membrane. The sign of the electrogenicity is considered positive when the change in dipole momentum is equivalent to a shift of a positive change in the proton transporting direction of the membrane [30].

3. Results and discussion

Determination of pK_a of the proton acceptor Asp 85 in the wild-type BR, bleached BR and retinal deficient BR was made from spectral titration in the pH range 1.5-10. To observe the minor changes in the spectra, the difference spectra (fig. 1A) were used. They were obtained after subtracting the spectrum measured at pH 7. The relative amplitude change calculated at two wavelengths 560 and 640 nm was plotted and titration curves were fitted to the points (fig. 1B).

For the wild-type BR the fitted apparent pK_a was 2.9, with a Hill coefficient of 2 protons, as determined earlier [32, 33]. For the bleached BR and retinal deficient BR the fitted apparent pK_a value increases to 3.6 in the bleached with a Hill coefficient 1.7 protons and to 4.7 in the retinal deficient BR with Hill coefficient 1.3 protons. These shifts show that after adding back the retinal to the samples the surrounding of the proton acceptor is changed compared with wild-type BR.

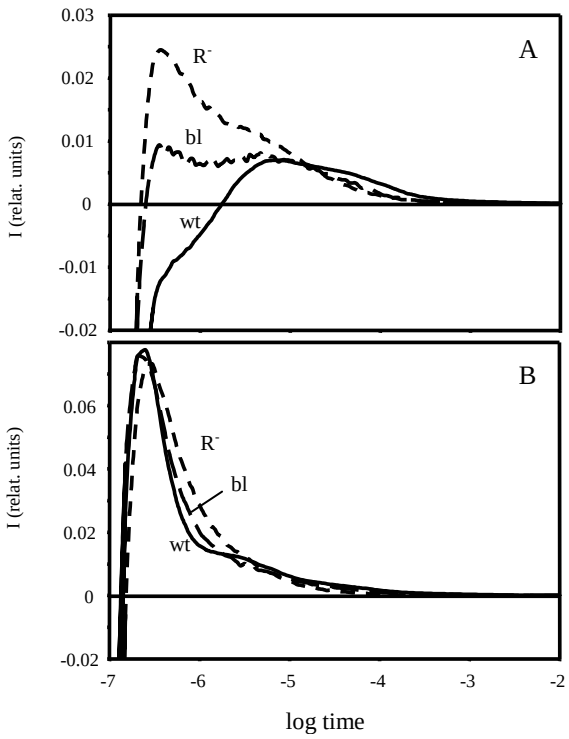

Fig. 2. Electric signal measured on oriented sample of wild-type, bleached and retinal deficient BR in 100 mM NaCl with 25 mM MES for the pH 7 (A) and 25 mM TRIS for the pH 9 (B).

To understand better the apparent pH shift of the reconstructed sample, electric signal measurements were performed on oriented gel samples at pH 6, 7 (fig. 2A) and 9 (fig 2B). This is a very sensitive tool to determine the pH of the suspension at which the wild-type BR works [2].

The electric measurements do not give information about the proton release or uptake step but show that the transfer of protons from one side of the membrane to the other occurs in well-determined steps. The electrogenicity of the photocylce intermediate, with the exception of the N intermediate, are pH independent. This indicates that the charge motion inside the protein during the proton transport steps, are the same for the whole studied pH

range. The location of charge transfer, during a particular transition between the intermediates, is pH independent. Hence the change configuration of each intermediate is pH independent.

In BR the electro-genicity of intermediate K was negative, the L also negative and about two times larger, resulting in a fast negative signal, which crosses the zero line, becoming positive in several microseconds. The positive current correspond the rise of M intermediate [30].

Although the external pH was identical for all three samples the bleached BR signal at pH 7 exhibited identical signal to that of wild-type BR measured at pH 8.5 [2] and the retinal deficient BR signal at pH 7 corresponded to that of wild-type BR measured at pH 9.

Although the upward shift of the proton acceptor pK_a suggested that the photocycle would correspond to a lower pH of the wild-type BR, we got an inverse effect, which shows that the position of the retinal in the reconstructed BR is different from that of the wild-type. It is important to note that in the retinal deficient BR, where the protein did not have retinal before, this shift is bigger.

4. Conclusion

The results obtained from spectroscopic and electric signal measurements indicate that the added retinal is not able to rebind in the same position in the reconstructed BR as compared with the wild-type sample. The importance of the above study is in the fact that the bacteriorhodopsin is considered one of the most potent material in bioelectronical application.

Acknowledgements

The National Science Research Fund of Hungary OTKA T048706, Romanian National University Research Council CNCSIS A63-192 and the Domus Hungarica supported this work

REFERENCES

1. W. Stoeckenius, R. H. Lozier, and R. A. Bogomolni, Biochim. Biophys. Acta, **505** (1979) 215-278.
2. W. Stoeckenius and R. A. Bogomolni, Annu. Rev. Biochem., **51** (1982) 587-616.
3. J. K. Lanyi, Comparative biochemistry: bioenergetics, Elsevier, Amsterdam, 1984, pp. 315-350

4. H. Luecke, B. Schobert, H. T. Richter, J. P. Cartailler, and J. K. Lanyi, J. Mol. Biol., **291** (1999) 899-911.
5. C. Gergely, L. Zimányi, and G. Váró, J. Phys. Chem. B, **101** (1997) 9390-9395.
6. K. Ludmann, C. Gergely, A. Dér, and G. Váró, Biophys. J., **75** (1998) 3120-3126.
7. G. I. Groma, A. Colonna, J. C. Lambry, J. W. Petrich, G. Váró, M. Joffre, M. H. Vos, J. L. Martin. Proc. Natl. Acad. Sci. USA **101** (2004) 7971-7975
8. V. Z. Spassov, H. Luecke, K. Gerwert, D. Bashford, J. Bol. Biol. **312** (2001) 203-219
9. G. Váró, J. K. Lanyi, Biochemistry **29** (1990) 2241-2250
10. D. Oesterheld, J. Tittor, E. Bamberg, J. Bioenerg. Biomembr. **24** (1992) 181-191
11. J. K. Lanyi, Int. Rev. Cytol. **187** (1999) 161-202
12. G. Váró, J. K. Lanyi, Biophys. J **56** (1989) 1143-1151
13. Z. Dancsházy and B. Karvaly, FEBS. Lett., **72** (1976) 136-138.
14. E. Bamberg, N. A. Dencher, A. Fahr, and M. P. Heyn, Proc. Natl. Acad. Sci. USA, **78** (1981) 7502-7506
15. L. A. Drachev, A. D. Kaulen, and V. P. Skulachev, FEBS Lett., **178** (1984) 331-335.
16. M. Holz, M. Lindau, and M. P. Heyn, Biophys. J., **53** (1988) 623-633
17. L. Keszthelyi and P. Ormos, FEBS Lett., **109** (1980) 189-193.
18. L. Keszthelyi and P. Ormos, J. Membr. Biol., **109** (1989) 193-200.
19. E. Bamberg, A. Fahr, Ann NY Acad. Sci. **358** (1980) 324-327
20. D. Oesterhelt, L. Schuhmann, and H. Gruber, FEBS. Lett., **44** (1974) 257-261
21. I. Rousso, Y. Gat, A. Lewis, M. Sheves, and M. Ottolenghi, Biophys. J., **75** (1998) 413-417.
22. D. Oesterhelt and L. Schuhmann, FEBS. Lett., **44** (1974) 262-265
23. M. Rehorek and M. P. Heyn, Biochemistry., **18** (1979) 4977-4983.
24. D. Oesterhelt and W. Stoeckenius, Methods. Enzymol., **31** (1974) 667-678.
25. D. Oesterhelt, L. Schuhmann, and H. Gruber, , FEBS. Lett., **44** (1974) 257-261.
26. I. Rousso, Y. Gat, A. Lewis, M. Sheves, and M. Ottolenghi, Biophys. J., **75** (1998) 413-417.
27. P. C. Mowery, R. H. Lozier, Q. Chae, Y. W. Tseng, M. Taylor, and W. Stoeckenius, Biochemistry, **18** (1979) 4100-4107.
28. A. Dér, P. Hargittai, and J. Simon, J. Biochem. Biophys. Methods., **10(5-6)** (1985) 295-300.
29. C. Gergely, C. Ganea, G. I. Groma, G. Váró, Biophys J. (1993) **65**:2478-2483
30. K. Ludmann, C. Gergely, A. Dér, and G. Váró, Biophys. J., **75** (1998) 3120-3126.
31. R. H. Lozier, A. Xie, J. Hofrichter, and G. M. Clore, Proc. Natl. Acad. Sci. U. S. A., **89** (1992) 3610-3614.
32. S. P. Balashov, E. S. Imasheva, R. Govindjee, and T. G. Ebrey, Biophys. J., **70** (1996) 473-481.
33. S. P. Balashov, E. S. Imasheva, R. Govindjee, M. Sheves, and T. G. Ebrey, Biophys. J., **71** (1996) 1973-1984.

STUDIA UNIVERSITATIS BABEŞ-BOLYAI, PHYSICA, LII, 2, 2007

ELECTRON IMPACT IONIZATION OF Kr AND Xe

R. I. CAMPEANU*

ABSTRACT. Distorted wave models, which were successfully used in positron impact ionization studies, are applied to electron impact ionization of Kr and Xe. When combined with the 'maximum interference' exchange approximation, our models CPE4 and DCPE4 give results which are in good agreement with the experiments.

1. Introduction

Electron impact single ionization of light noble gas atoms is one of the most important testing grounds for theoretical models. This is because a large number of experiments are available and because ionization processes play an important role in many areas of research, such as plasma physics or astrophysics.

Most experiments measuring total ionization cross sections [1,2] are in agreement with each other, but on the theory side work is still needed for atoms heavier than helium. For the heaviest noble gases (Kr and Xe) there are very few total ionization cross section calculations. The existing theoretical data were produced with the distorted wave Born exchange approximation [3], with the coupled-channel-optical (CCO) model [4] and with a Born approximation using an ejected electron Coulomb wave function orthogonalized to all occupied atomic orbitals [5] (to be referred in this letter as BCO). All these methods produced total ionization cross sections which are significantly higher than the experimental data.

Our theoretical work on positron impact ionization of atoms and molecules was based on the use of several simple distorted-wave models [6,7]. We found that two of these models (CPE4 and DCPE5) produce results which are in good agreement with the experiments for hydrogen and all the noble gases. Recently we have employed these models, in conjunction with the 'maximum interference' exchange approximation [8], in the case of electron impact ionization of He, Ne and Ar. We found that models CPE4 and DCPE produced the best agreement with the experiments [9].

* Department of Physics and Astronomy, York University, 4700 Toronto, ON Canada, e-mail: campeanu@yorku.ca

In this Letter we examine the possibility of employing the same distorted-wave models in the case of positron impact ionization of Kr and Xe.

2. Theory

In this paper the electron impact ionization total cross section are calculated with:

$$Q(E_i) = \frac{16}{\pi E_i} \int_0^{E/2} dE_e \sum_{lilelf} (2L+1) I(l_i l_e l_f) \qquad (1)$$

where l_i l_e l_f represent the orbital angular momentum quantum numbers of the incident, ejected and scattered electrons respectively, E_i is the energy of the incident electron, E_e the energy of the ejected electron, and $E = E_i - I = E_e + E_f$ is the total energy of the scattered electrons, where I is the ionization energy.

In the 'maximum interference' model [8] $I(l_i\, l_e\, l_f)$ is written as:

$$I(l_i\, l_e\, l_f) = |F|^2 + |G^0|^2 - |F||G^0| \qquad (2)$$

where the singlet exchange amplitude G^0 is defined by the same expression as the direct scattering amplitude F, but with the energies of the ejected and scattered electrons interchanged. The scattering amplitudes are function of the channel radial wave functions, which were calculated numerically for various scattering potentials.

The Coulomb plus plane waves with full energy range (CPE) model considers that both the ejected and scattered electrons see the residual atomic ion as a positive single charge:

$$V_e = V_f = -\frac{1}{r}, \text{ while } V_i = 0 \qquad (3)$$

The CPE4 model includes the repulsion between the ejected and scattered electrons:

$$V_e = V_f = -\frac{1 - E_e / E_{ef}}{r}, \text{ while } V_i = 0 \qquad (4)$$

with E_{ef} given by:

$$E_{ef} = E_e + E_f - 2\,(E_e\, E_f)^{1/2} \qquad (5)$$

Thus, in both CPE and CPE4 the incident electron is represented as a plane wave, while the ejected and scattered electrons are represented as Coulomb waves.

The Distorted-wave CPE model (DCPE) is different from CPE only in the representation of the incident electron, which moves in the atomic static and polarization potentials:

$$V_i = V_{st} + V_{pol} \qquad (6)$$

In our paper on electron impact ionization of He, Ne and Ar [9] we found that CPE4 and DCPE produce best agreement with the experiment. In this work we included the use of DCPE4, a model which in our previous work [7,9] produced ionization cross sections below those of CPE4 and below the experimental measurements. Model DCPE4 is different from CPE4 only in the representation of the incident electron, which is now given by equation (6).

Details of the numerical work were presented in a previous paper [10]. For heavy targets, such as Kr and Xe, we examined carefully the effect of refining the integration radial mesh.

3. Results and discussion

Table 1 and Figure 1 present our DCPE, CPE4 and DCPE4 total ionization cross-sections for krypton. In addition to the current data in Figure 1 we included two of the existing sets of experimental data and the CCO [4] and BCO [5] model results.

We find that all theories overestimate the ionization cross sections for impact energies between 100 and 300 eV. The highest results are those obtained by McCarthy and Zhou [4] and the lowest by our model DCPE4. For impact energies below 100 eV our models CPE4 and DCPE4 fall below the experiment, while DCPE, BCO and CCO are significantly above the experiment. At high impact energies our models produce cross sections just below the experiment, while CCO and BCO are above the experiment.

From all the theoretical results of Figure 1 the best agreement with the experiments is given by DCPE4 for impact energies between 100 and 480 eV. Unfortunately both DCPE4 and CPE4 results fall below the experiment below 100 eV and over 480 eV. In the case of lighter noble gases our CPE4 results fell under the experiment at very low impact energies but were in perfect agreement with the experiment at 500 eV [9].

Tables 2 and Figure 2 show our total ionization cross-sections for xenon. All observations related to Figure 1 apply to Figure 2 except that the overestimation of the theoretical cross sections at intermediate impact energies is more pronounced. The distorted-wave cross sections of Younger [3] are slightly higher than the CCO results and were not included in the graph.

As in the case of krypton, the best model for xenon at intermediate impact energies is DCPE4. Although the DCPE4 results fall under the

experiment for impact energies below 50 eV, it is interesting to note that the agreement with the experiment at these very low impact energies is much better than in the krypton case. At impact energies higher than 400 eV the DCPE4 cross sections gradually fall under the experiment. Model CPE4 produces results which are very close to the DCPE4 results. Only around 100 eV the CPE4 data disagree with the experiment much more than the DCPE4 results.

Model DCPE4 contains a final state representation which includes the electrostatic interaction between the ejected electron and the scattered positron and a description of the incident electron in the atomic static and polarization fields. However this description is not complete. Electron exchange is missing in these channel representations and is added only in the 'maximum interference' approximation in the ionization cross section formula.

For these heavy noble gases one would also expect relativistic effects to be important. We did not consider them in this work, but the paper of McCarthy and Zhou [4] showed that relativistic effects only slightly lower the total ionization cross sections.

Table 1.

Electron-krypton ionization cross sections (in 10^{-16} cm^2) in the DCPE, CPE4 and DCPE4 models. The 200 and 500 eV total cross sections also include small contributions from 3s, 3p, and 3d orbitals.

Energy(eV)	Kr(4p)			Kr(4s)			Kr(total)		
	DCPE	CPE4	DCPE4	DCPE	CPE4	DCPE4	DCPE	CPE4	DCPE4
30	2.745	1.673	0.764				2.745	1.673	0.764
40	3.643	2.191	1.382				3.643	2.191	1.382
60	4.015	2.949	2.029	0.819	0.368	0.356	4.834	3.317	2.385
80	3.862	3.347	2.460	0.992	0.606	0.574	4.854	3.953	3.034
100	3.632	3.515	2.620	1.035	0.798	0.727	4.667	4.313	3.347
200	2.420	2.947	2.478	0.777	0.891	0.872	3.200	3.842	3.352
500	0.818	0.894	0.881	0.258	0.315	0.302	1.090	1.226	1.193

Table 2.

Electron-xenon ionization cross sections (in 10^{-16} cm^2) in the DCPE, CPE4 and DCPE4 models. The 200 and 500 eV total cross sections also include small contributions from 4s, 4p and 4d orbitals.

Energy(eV)	Xe(5p)			Xe(5s)			Xe(total)		
	DCPE	CPE4	DCPE4	DCPE	CPE4	DCPE4	DCPE	CPE4	DCPE4
20	3.921	1.851	1.159				3.921	1.851	1.159
40	6.819	4.257	3.550				6.819	4.257	3.550
60	6.861	5.952	4.501	1.600	0.797	0.938	8.461	6.749	5.439
80	6.216	5.765	5.090	1.590	1.672	1.308	7.806	7.437	6.398
100	5.550	5.747	5.083	1.526	1.544	1.281	7.076	7.291	6.364
200	3.213	3.739	3.577	0.908	1.176	1.152	4.156	4.943	4.740
500	0.782	0.862	0.873	0.219	0.287	0.244	1.070	1.235	1.156

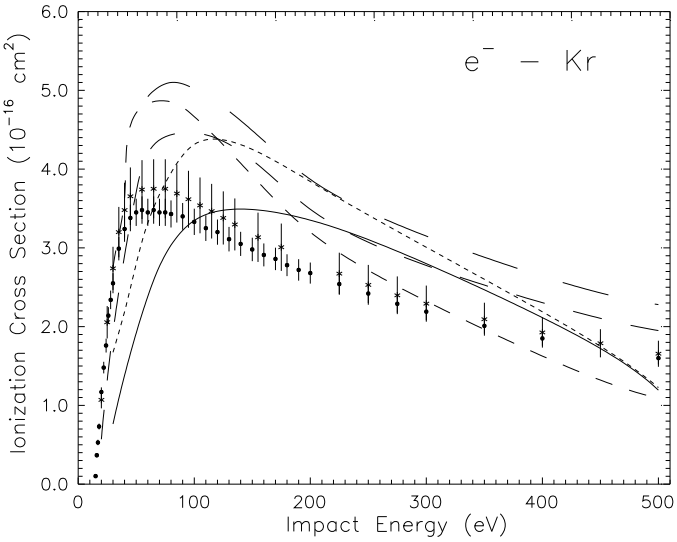

Fig. 1. Total cross-sections for electron impact ionization of krypton as a function of the electron impact energy. The experimental points are from Krishnakumar et al [1] (asterixes) and Rejoub et al. [4] (full circles). The shortest dashed line corresponds to CPE4, the solid line to DCPE4, the long-dashed lines in increasing size of the dash to DCPE, BCO [5] and CCO [4].

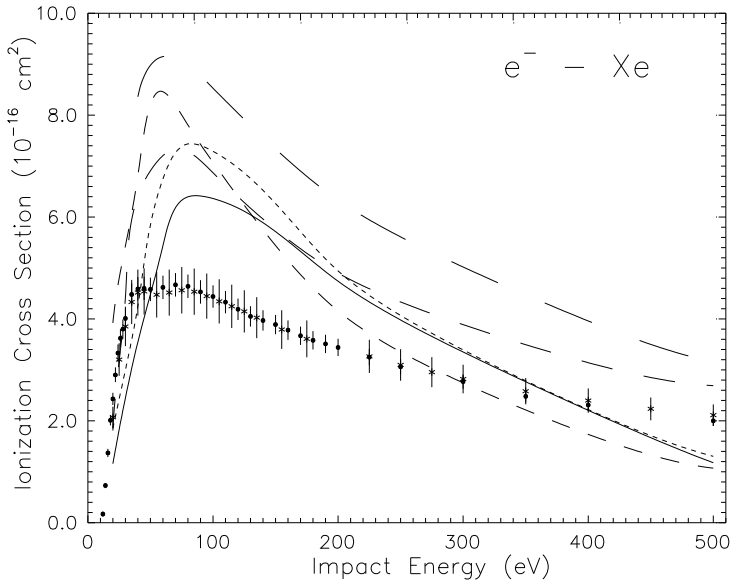

Fig. 2. Same as Figure 1 but for electron impact ionization of xenon.

4. Conclusions

This work completes our study of the electron impact ionization of noble gases. We found that for the heaviest noble gases two relatively simple distorted-wave models, CPE4 and in particular DCPE4, can produce good agreement with the total ionization cross section measurements, when combined with the 'maximum interference' exchange approximation.

Our theoretical models do not contain a complete description of the ionization channels particularly in relation to the exchange effects. However, they contain an explicit account of the pre and post-collision effects.

We conclude that among all models examined, CPE4 produces the best overall agreement with experiments, both for positron and electron impact. In the positron impact case a small improvement was obtained with DCPE5 [6], while in the electron case the improvement was obtained with models DCPE for Ne and Ar [9] and with model DCPE4 for Kr and Xe.

5. Acknowledgement

This research was supported by a grant from the Natural Sciences and Engineering Council of Canada (NSERC).

REFERENCES

1. E.Krishnakumar, S.K.Srivastava, J.Phys.B : At.Mol.Opt.Phys. **21** (1988) 1055
2. R. Rejoub, B. G. Lindsay, R. F. Stebbings, Phys.Rev.A**, 65** (2002) 042713
3. S.M.Younger, Phys.Rev.A **37** (1988) 4125
4. I.E.McCarthy, Y.Zhou, Phys.Rev.A **49** (1994) 4597
5. P.L.Bartlett, A.T.Stelbovics, At.Data&Nucl.Data, **86** (2004) 235
6. R. I. Campeanu, R. P. McEachran, A. D. Stauffer, Nucl.Instrum.Meth.Phys.Res. B **192** (2002) 146
7. R. I. Campeanu, R. P. McEachran, A. D. Stauffer, Can.J.Phys. **79** (2001) 1231
8. R.K.Peterkop, Zh.Eksp.Teor.Fiz. **41** (1961) 1938
9. R.I.Campeanu, to appear in Phys.Lett.A (2007)
10. R. I. Campeanu, R. P. McEachran, A. D. Stauffer, Can.J.Phys. **74** (1996) 544

STUDIA UNIVERSITATIS BABEŞ-BOLYAI, PHYSICA, LII, 2, 2007

HEAT TREATMENT EFFECT ON NANOCRYSTALLINE MINERAL PHASE OF BONES

S. SIMON[1], H. MOCUTA[1], M. BĂCIUŢ[2], G. BĂCIUŢ[2], V. COMAN[3], P. PRODAN[2], ŞT. I. FLORIAN[2]

ABSTRACT. The aim of the present study is to investigate the structural changes determined by heat treatment of different bones in order to prove the possibility to obtain hydroxyapatite (HAP) powder usable for biomedical coating applications. X-ray diffraction (XRD) technique was employed to check the crystalline structure of samples. XRD analysis reveals pure HAP after heat treatment applied at 1200℃.

Introduction

Bone mineral is an important biomaterial resource. Accurate measurement of bone crystal alteration, both in structure and composition, has been a focus of biomaterial research for several years [1]. Heat treatment was used to deproteinate bone mineral for use in osteoimplantation, since natural hydroxyapatite with the organic matrix removed is potentially a better basis for bone grafting than synthetic materials [2]. However, the usefulness of this material relies on the retention of biogenic crystallite characteristics throughout the preimplantation treatment process.

Changes to the biogenic composition and structure of bone mineral following heat treatment at different temperatures could affect its efficacy in these procedures. It is important to know the temperature at which crystallites begin to change and how rapid the alteration can be. Previously, X-ray diffraction was used to determine changes to the mineral phase of bone during heating [3]. Results have shown that there is a generalised trend toward a more crystalline phase of hydroxyapatite at temperatures up to 1000^{o}C.

Hydroxyapatite (HAP) is one of the inorganic components of the hard tissues such as bones and teeth. HAP is a calcium phosphate-based

[1] Babeş Bolyai University, Faculty of Physics and Institute for Interdisciplinary Experimental Research, 400084 Cluj-Napoca, Romania
[2] Iuliu Haţieganu University of Medicine and Pharmacy, Department of Cranio-Maxillofacial Surgery, 400029 Cluj-Napoca, Romania
[3] Raluca Ripan Institute for Research in Chemistry, 400294 Cluj-Napoca, Romania

bioceramic ($Ca_{10}(PO_4)_6(OH)_2$), which has been used in medicine and dentistry because of its excellent biocompatibility with human tissue [4] and has been widely used in dental implants [5], alveolar bridge augmentation, orthopaedics [6] and maxillofacial surgery [7]. HAP is known to be bioactive, osteoconductive, non-toxic, non-inflammatory and non-immunogenic agent [8, 9]. Considering the numerous application of HAP in biomedical fields, various synthesis techniques have been developed [10]. The effects of heating and burning have previously been studied using techniques such as XRD with the aim of discerning a characteristic signature of crystal change [1].

In the present investigation, an attempt was made to obtain through heat treatment method HAP from bones of different provenance. The study aims to evidence by means the changes to bone mineral during heating at temperatures up to 1200^{o}C using X-ray diffraction analysis.

Experimental

The investigated samples are cattle, turkey and chicken bones. In order to degrease the bones, they were kept for 48 hours in acetone and for 30 minutes in ethylic ether. The solvent was removed by heating the samples at 40ºC.

X-ray diffraction (XRD) analysis was carried out both on untreated and heat treated powdered bones. The samples were thermal treated in an electric furnace at 500 and 1200^{o}C, in air, for 2 hours. Wide angle-X-ray scattering traces were recorded on a Shimadzu XRD – 6000 diffractometer using Cu Kα (λ = 1.5405 Å) radiation.

Samples were analysed over a 2θ range between 10° and 70° with a sampling interval of 0.02°. Crystallographic identification of the phases was accomplished by comparing the experimental XRD patterns to standard inorganic crystal structure data.

Results and discussion

The XRD analysis indicates an apparent similarity concerning the structure of the three bone samples (Fig. 1). The major reflections occur from the planes (002) at 25.8^o, (210) at 29 ^{o}, (211), (112) and (300) leading to the triplet between 32^o and 33.5^o, (310) at 39.5 ^{o}, (222) at 46.5^o, (213) at 49^o and (323) at 64^o [11]. They are certain signature for hydroxyapatite crystals. They differ very slight in the linewidth, indicating crystal size between 14.2 and 19 nm. The crystal size was estimated from diffractograms using the Scherrer formula [12] for the (002) reflection. These values denote the nanoscale ordered structure of the samples.

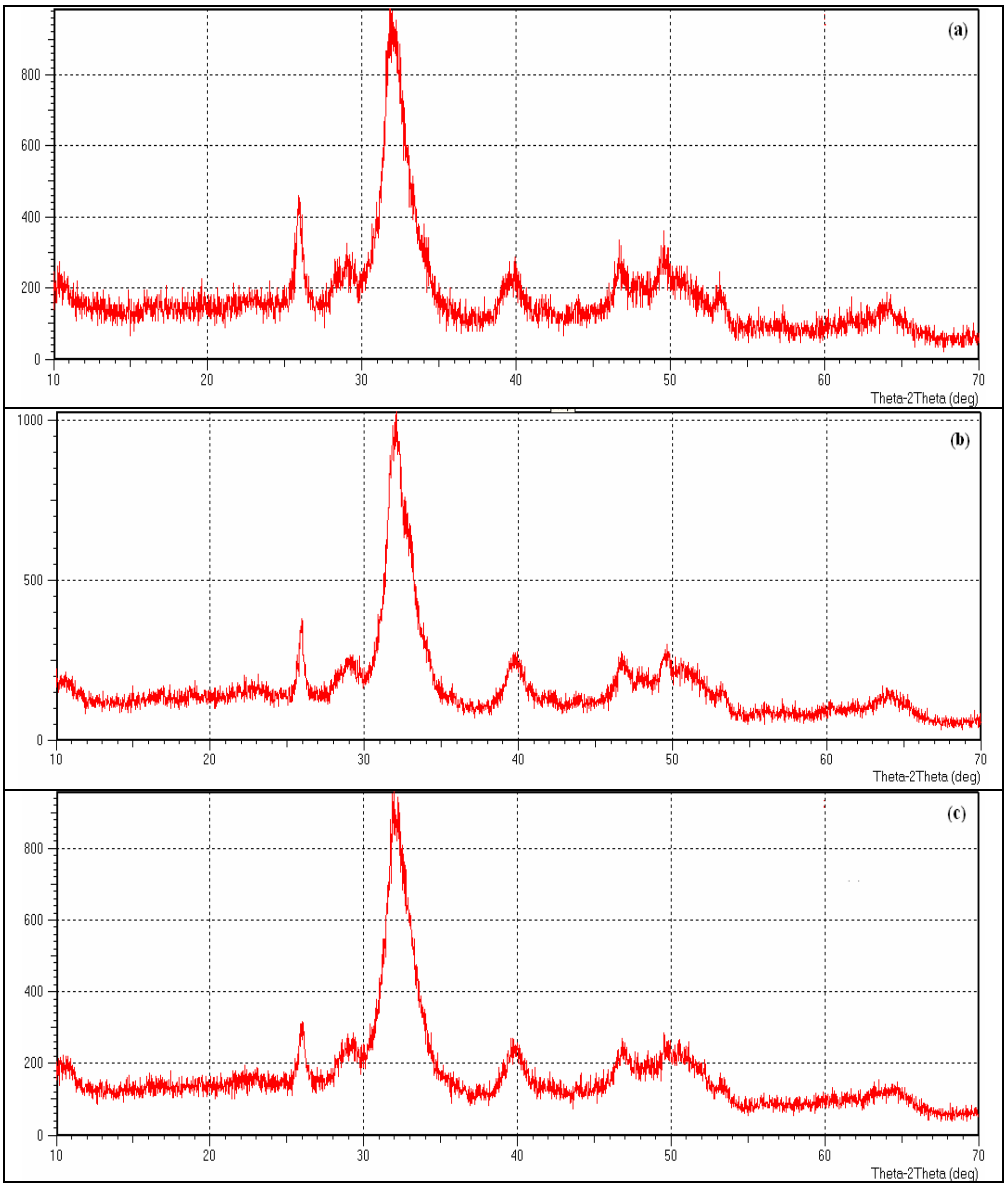

Fig. 1. XRD patterns of bone samples of different orygins
(a-cattle, b-turkey and c-chicken)

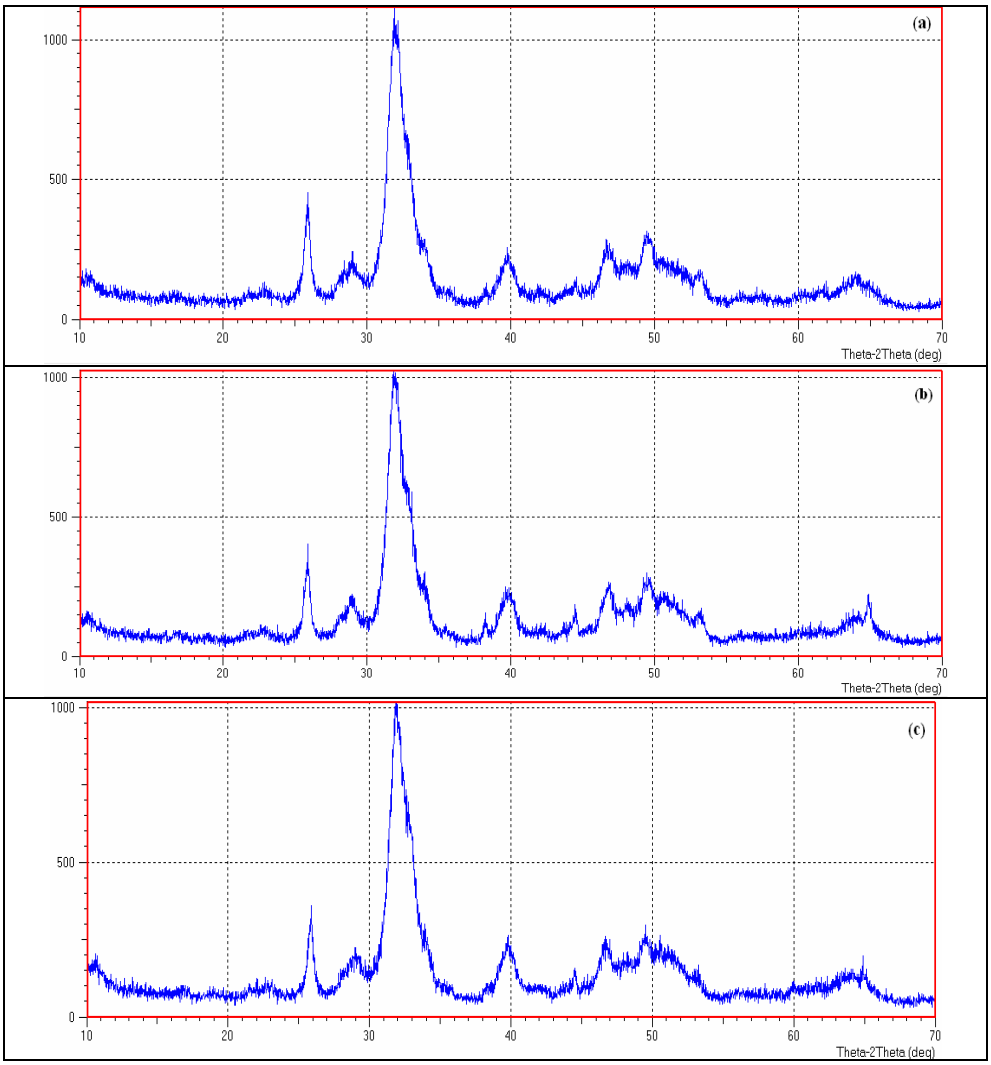

Fig. 2. XRD patterns of bone samples heat treated at 500^{o}C for 2 hours (a-cattle, b-turkey and c-chicken)

Around one third of bone is composed of organic compounds, of which 90 to 95% is collagen, the rest being non-collagenous proteins. Collagen is a fibrous protein which provides the bone with strength and flexibility. The X-ray diffractogram for pure collagen consists of a broad diffraction pattern at $2\theta = 10^{o}$ and a characteristic large peak at $2\theta = 23^{o}$. These features are not well evidenced in the XRD patterns of the investigated bone samples.

The heat treatment applied at 500^{o}C for 2 hours practically does not affect the structure of the samples, as far as X-ray diffraction analysis can detect. However, one discerns a weak narrowing of all diffraction peaks, which reflects an effect on the samples crystallinity. The bone samples architecture is plenty affected by the 2 hours heat treatment applied at 1200^{o}C. As can be seen from the diffraction patterns (Fig. 3), the inorganic phase of bones is now organised by the account of the thermal energy in a well defined crystalline structure corresponding to the pure mineral hydroxyapatite (Fig. 4). This structural evolution as a consequence of the applied heat treatments points out the high similarity of the animal bone tissue of different origins.

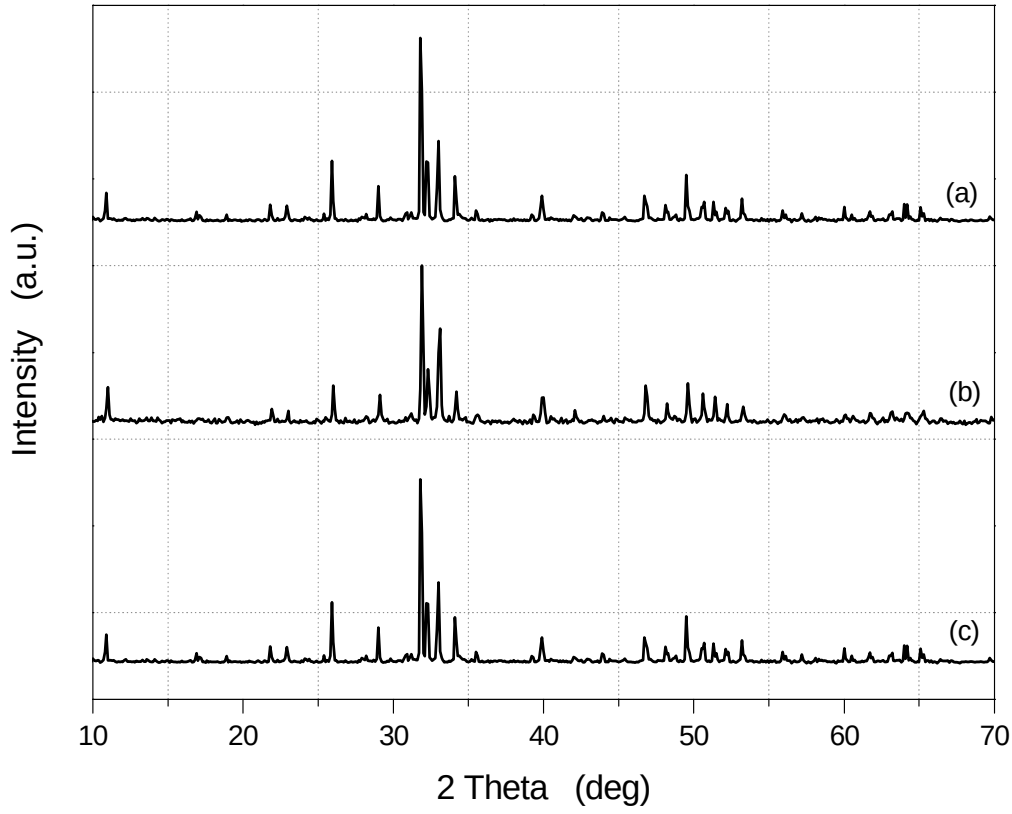

Fig. 3. XRD patterns of bone samples heat treated at 1200^{o}C for 2 hours (a-cattle, b-turkey and c-chicken)

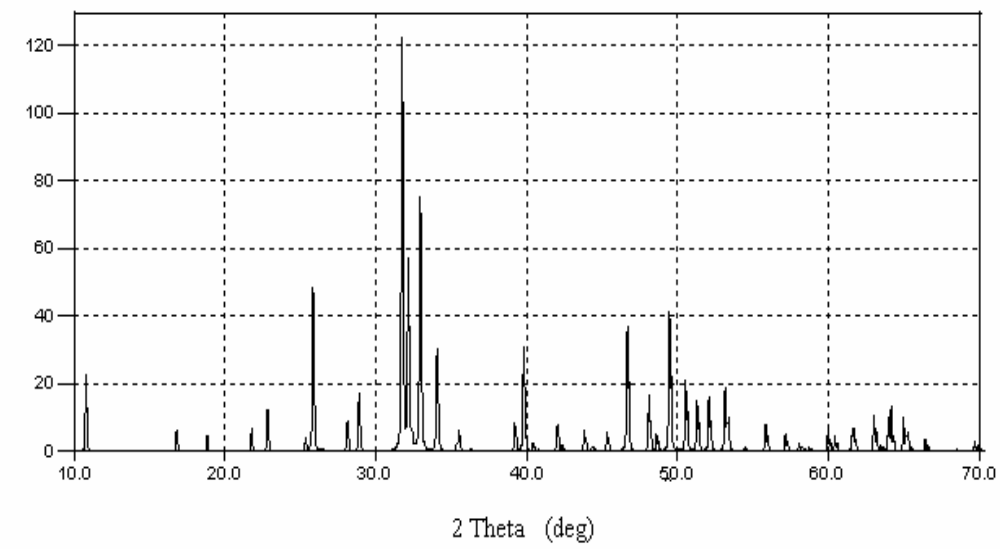

Fig. 4. XRD pattern of pure mineral hydroxyapatite [13].

Conclusions

Wide angle XRD analysis shows a high structural similarity of the investigated bone samples. The bones consist of nanosized crystals (14.2 - 19 nm). XRD does not detect significant changes in the structure of bone samples heat treated at 500^{o}C, excepting a faint increase of the crystallinity. After the heat treatment applied at 1200^{o}C the structure of all samples, regardless of the bone origin is highly ordered like pure mineral hydroxyapatite.

REFERENCES

1. J.C. Hiller, T.J.U. Thompson, M.P. Evison, A.T. Chamberlain, T.J. Wess, Biomaterials, 24, 5091 (2003)
2. S. Guizzardi, M. Raspanti, D. Martini, R. Scandroglio, P. Govoni, A. Ruggeri, Biomaterials, 16, 931 (1995)
3. K.D. Rogers, P. Daniels, Biomaterials, 23, 2577 (2002)
4. L. L. Hench, Biomaterials, 19, 1419 (1998)

5. K. Soballe, S. Overgaard, J. Bone Joint Surg., 78B, 689 (1996)
6. M. Zablotsky, J. Dent. Symp., 1, 70 (1993)
7. R. J. Cronin, L. J. Oesterle, D. M. Ranly, Int. J. Oral Maxillofac. Implants, 9, 55 (1994)
8. L. L. Hench, J. Wilson, Science, 226, 630 (1984)
9. J. Currey, Nature, 414, 699 (2001)
10. K. Prabakaran and S. Rajeswari, Trends Biomater. Artif. Organs, 20, 20 (2006)
11. A.C. Tas, Powder Diffract., 16, 2, 102 (2001)
12. H. P. Klug, L.E. Alexander, X-ray Diffraction Procedures. John Wiley, New York 1954
13. K. Sudarsanan, R.A. Young, Acta Crystallogr. B , 24, 34, 1401 (1978)

STUDIA UNIVERSITATIS BABEŞ-BOLYAI, PHYSICA, LII, 2, 2007

STRUCTURAL CHARACTERISATION OF GADOLINIUM DOPED *0.875$Bi_2O_3$0.125GeO_2* NON- AND POLYCRYSTALLINE SYSTEM

O. PONTA*, D. A. UDVAR, S. SIMON

ABSTRACT. The Bi_2O_3-rich glass sample of the following composition *0.005·Gd_2O ·0.995 (0.875$Bi_2O_3$0.125GeO_2)* was prepared by rapid cooling of the melts. The polycrystalline sample was obtained after 24 hours heat treatment of the glass sample. Glass and polycrystalline samples were characterized by DTA, X-ray, infrared (IR) and Raman spectroscopies.

The developed crystalline phase formed after the heat treatment applied was identified as being $Bi_{12}GeO_{20}$. Structural model for the investigated glass sample is suggested on the basis of IR and Raman spectroscopic investigations on its crystalline counter part.

Keywords: Local structure; glass; vitroceramic; XRD; IR spectroscopy; Raman spectroscopy.

1. Introduction

Glasses with a high content of heavy metals, are intensively investigated because of their properties such as high density, high refractive index, excellent IR transmission and high polarisability [1–5]. All of these properties are exploited in applications such as thermal and mechanical sensors [5], waveguides in non-linear optics [6], scintillation detectors in high-energy physics [6,7]. The investigation of bismuth germanate is interesting due to the fact that both GeO_2 and Bi_2O_3 are glass former oxides and on the other hand, because both bismuth and germanium ions are known to have more than one stable coordination: GeO_4, GeO_6 and BiO_3, BiO_6 respectively and also for the presence of $Bi_{12}GeO_{20}$ phase [8] at high bismuth concentration.

There are at least two reasons to introduce paramagnetic ions into diamagnetic glass matrices, such as bismuth–germanate. Firstly, the glass formed may acquire new magnetic properties and, secondly, they may be studied by electron paramagnetic resonance (EPR) spectroscopy, one of the most powerful techniques for local order investigation [9].

* Faculty of Physics, Babes-Bolyai University, M. Kogalniceanu no 1, 400084 Cluj-Napoca, Romania

Obtained by quick undercooling of melts, glasses are metastable systems in which different relaxation processes tend to decrease the frozen in structural disorder. Structural relaxation of glasses may involve local rearrangements of atoms or, under certain conditions, may lead to a partial or complete crystallization of the glass.

2.Experimental

The glass sample of composition corresponding to *0.005·Gd_2O ·0.995 (0.875$Bi_2O_3$0.125GeO_2)* system was prepared by using reagent grade chemicals Gd_2O_3, GeO_2 and Bi_2O_3. The components were mixed thoroughly to prepare the batch which was then melted at 1250℃ and air quenched at room temperature to obtain the glass.

The heat treatment temperature at 600℃ was establi shed by using DTA data.

The X-ray measurements were performed with a Bruker Advance X-ray difractometer.

The IR spectra of the samples were recorded in the wavenumber range 400-1000 cm^{-1} at room temperature. The measurements were made by IR Equinox 55 spectrometer using “KBr pellet” technique, with the maximum resolution of 0.16 cm^{-1}.

The measurements of the Raman spectra were performed on a LabRam integrated Raman system by an external laser with an emission wavelength of 514.5 nm. The Raman spectra were recorded at the room temperature in the wavenumber range 200 to 1000 cm^{-1}.

3. Results and discussion

The as prepared glass sample was found to be non-crystalline.

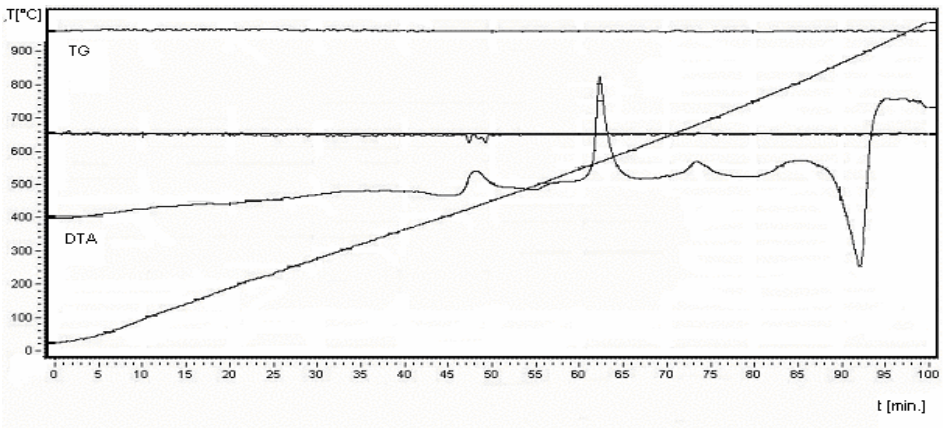

Figure 1. DTA curves for glass sample

The DTA method was used to establish the heat treatment temperature for obtaining polycrystalline sample. Using the DTA curve (fig.1) the heat treatment temperature was settled at 600℃. The gla ss sample was heat treated at this temperature for 24 hours.

The X-ray diffractogram of the vitroceramic sample (fig. 2) shows that in the glass matrix only a single crystalline phase, identified as beeing $Bi_{12}GeO_{20}$ [8] was developed. This crystalline phase is a body-centred cubic one, with the spatial group I23 (197) having the following parameters: a=b=c=10.147 Á and $\alpha = \beta = \gamma = 90^0$ and is formed by BiO_3, BiO_6 and GeO_4 units.

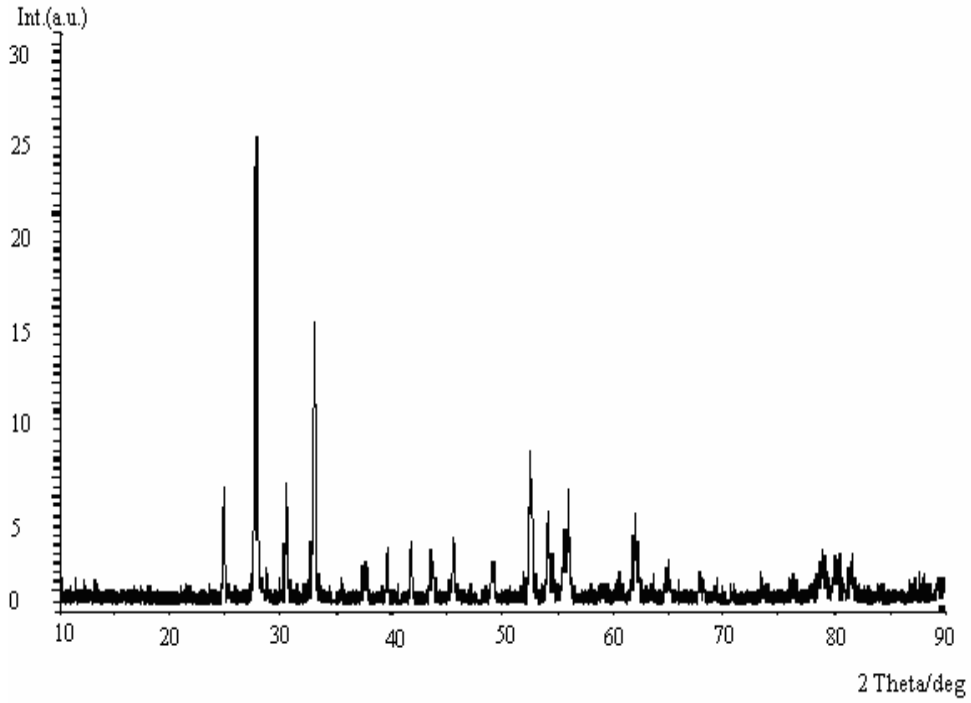

Figure 2. X-ray difractogram of the vitroceramic sample

The infrared spectra of the glass and vitroceramic samples are presented in figure 3.

The main spectroscopic features evidenced for the glass sample are three absorption bands centred at 470, 725 and 875 cm^{-1}. These infrared bands according to the literature [8,10] are characteristic for the Bi_2O_3–GeO_2 glass matrices. The overlapping band in the low wavenumber

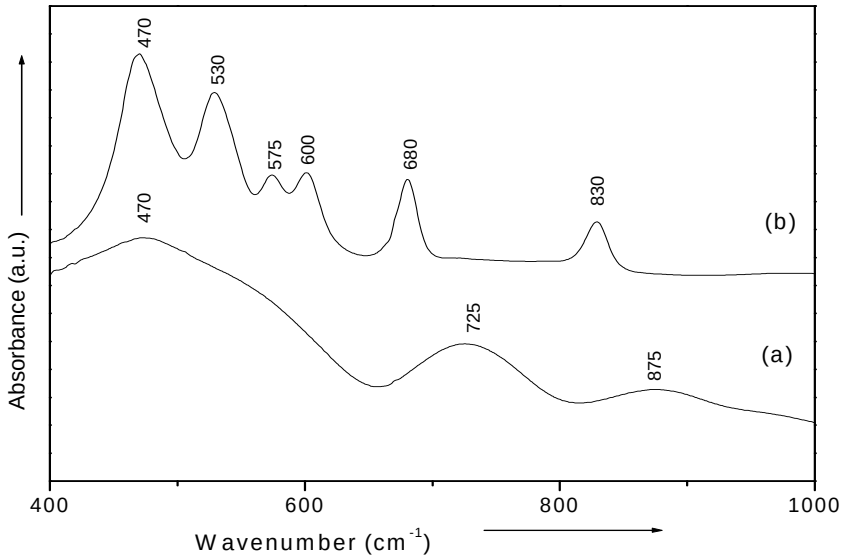

Figure 3. IR spectra before (a) and after (b) heat treatment

range, extended up to 650 cm^{-1}, with maximum at 470 cm^{-1} can be assigned to the stretching mode of Bi–O^- bonds in BiO_6 units [10-12,14,15] and the Bi–O^- total symmetric bending vibration in BiO_3 units [13,16].

The IR spectrum for the vitroceramic sample is better resolved, illustrated narrowing the bands and by the appearance of the three new bands in this wavenumber range. These bands are located around 530, 575, and 600 cm^{-1}. The band located at 530 cm^{-1} proved explicitly the presence of Bi–O^- bonds vibration in the BiO_6 units [14,15], while the bands around 575 and 600 cm^{-1} can be attributed to Bi–O^- double degenerate stretching vibrations in BiO_3 units [16].

The band which appears in the 725 cm^{-1} region of the glass spectrum, can be assigned to the rather localized Ge–O^- stretching modes of the metagermanate units (interconnected tetrahedral with two non-bridges GeO_4^{2-}) [17]. After the heat-treatment this band is shifted to lower wavenumbers, at 680 cm^{-1}, this position being specified in the literature like the most important support for the existence of GeO_6 polyhedra [14].

In the IR spectrum of the vitroceramic sample, the band around 875 cm^{-1} from the glass sample spectrum disappears, and a new band at 830 cm^{-1} is present. The existence of the absorption bands around 875 and 830 cm^{-1} show that the BiO_6 octahedral units, present in the glass sample, is transform by crystallization in the BiO_3 pyramidal units [19, 20]

The Raman spectra of the untreated and treated glasses are shown in the figure 4.

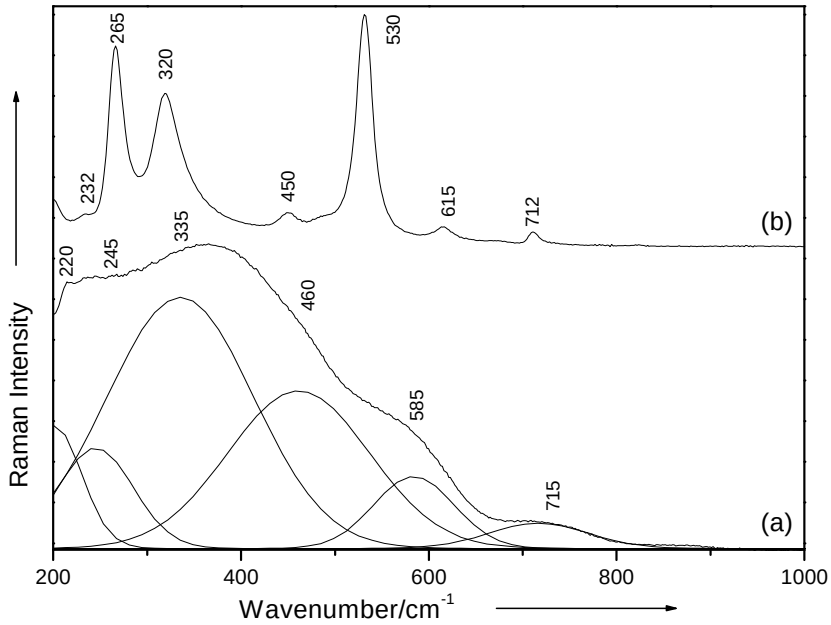

Figure 4. Raman spectra before (a) and after (b) heat treatment.

Like in IR spectrum, in Raman spectrum of untreated sample, are identify three spectral regions. The first one, low-wavenumber region (< 300 cm^{-1}), is attributed to the collective modes of local structure and heavy metal vibrational modes. The region between 300 – 650 cm^{-1} is attributed to the deformation of vibrational modes of a glass network structure with bridged oxygen and the last one (> 650 cm^{-1}) is attributed to the stretching vibrational modes of the glass network former.

The overlapping bands of the glass spectrum, was deconvoluted using a Gaussian band-shape to find out the most probable modes of vibrations. In the Raman spectrum, bands were assigned by comparing the experimental results with those of vitroceramic sample spectrum.

In the low-wavenumber region, the band around 220 cm^{-1} can be caused by the fact that the symmetry of individual structural units is lowered in the glassy solids due to the disorder and some break-down of selection rules should take place (can be attributed to Bi–O–Bi vibration in BiO_3 and/or BiO_6 polyhedra), but it is also very probable that this band is a laser line, not a real band.

The bands between 220 and 300 cm^{-1} appeared in the Raman spectrum due to the Bi–O vibrations. The band, at 245 cm^{-1} from the glass sample spectrum and the intense band at 265 cm^{-1} from the vitroceramic sample are due to the Bi–O vibrations in BiO_3 units [15].

The arising of the band around 335 cm^{-1} involve the Bi–O "breathing" vibration [19] in BiO_3 pyramidal units, but also can be given by Bi–O–Bi vibration of the interconnected distorted BiO_6 octahedral units [21]. In the Raman spectrum of vitroceramic sample, this band, shifted to 320 cm^{-1} is attributed to the symmetric stretching anion motion in angularly constrained cation-anion-cation configurations in BiO_6 polyhedra [21].

The bands around 450 and 460 cm^{-1} can be assigned to the Ge–O–Ge bonds bending mode between the GeO_4 units [22]. The shoulder, centered around 585 cm^{-1} is given by Bi–O–Bi vibration in distorded linked BiO_6 polyhedra [15]. The band around 530 cm^{-1} in the vitroceramic sample is attributed to the Bi–O–Bi stretching vibration, that could belong either to connected BiO_3 pyramidal units or to the BiO_3 linked to BiO_6 polyhedra [18].

The weak band centred at 615 cm^{-1} could be attributed to $Bi–O^-$ stretching vibration of non-bridging oxygen in the BiO_6 octahedral units [5].

The band which appear in the glass sample's spectrum, around 715 cm^{-1} is sifted to 712 cm^{-1} in the polycrystalline one and it can be assign to the symmetric stretching vibration of $Ge–O^-$ bands in GeO_4 units.

4. Conclusion

The glass and vitroceramic samples were investigated using the DTA, XRD, IR and Raman techniques. The heat treatment temperature was settled at 600℃ by using the DTA data. By X-ray diffraction was identified the $Bi_{12}GeO_{20}$ phase as a phase developed after 24h heat-treatment at 600℃. Were identified the structural units of the vitroceramic: BiO_3, BiO_6 and GeO_4. The structural characterisation of these materials was completed with IR and Raman measurements.

After heat-treatment at 600^{o}C the sample crystallizes and becomes opaque due to the nucleation and phase separation process.

Comparing to the untreated sample's spectra, where the bands are broad, with the IR and Raman spectra of the polycrystalline sample, where the bands are narrow and sifted to lower wavenumbers and also new bands appears and a better assigned of the glass bands have been noticed.

Agreement with the IR and Raman data by crystallization the GeO_6 units present in glass sample are converted in GeO_4 units and a part of BiO_6 units in BiO_3 pyramidal units.

REFERENCES

1. K. Ohura, M. Ikenaga, T. Nakamura, T. Yamamuro, Y.Ebisawa, T. Kokubo, Y. Kotoura, M. Oka, J. Appl.Biomater. 2 (1991) 153.
2. W.H. Dumbaugh, J.C. Lapp, J. Am. Ceram. Soc. 75 (9) (1992) 2315.
3. S. Hazra, A. Ghosh, Phys. Rev. B 51 (1995) 851.
4. Y. Dimitriev, V.T. Mihailova, J. Sci. Lett. 9 (1990) 1251.
5. S. Hazra, S.Mandal, A. Ghosh, Phys. Rev. B 56(13)(1997) 8021.
6. C. Stehle, C. Vira, D. Hogan, S. Feller, M. Affatigato, Phys. Chem. Glasses 39 (2) (1998) 836.
7. S.E. Van Kirk, S.W. Martin, J. Am. Ceram. Soc. 75 (4) (1992) 1028.
8. M.F. Carrasco, S.K. Mendiratta, L. Marques, A.S.B. Sombra, J. Mater. Sci. Lett. 21 (12) (2002) 963.
9. I. Ursu, Rezonanta Electronica de Spin, ed. Academiei, Bucuresti (1965).
10. P. Pernice, A. Aronne, M. Catauro, A. Maratto, J. Non-Cryst. Solids 210 (1997) 23- 31.
11. R. Iordanova, Y. Dimitriev, V. Dimitrov, S. Kassabov, D. Klissurski, J. Non-Cryst. Solids 204 (1996) 141- 150.
12. I. Ardelean, I. Todor, P. Pascuta, I. Bratu, Mod. Phys. Lett. B, 17, (8) (2003) 311-315.
13. D. Sreenivasu, V. Chandramouli, Bul. Matter. Sci., 23, (4), (2000), 281-284.
14. V. Dimitrov, Y. Dimitriev, A. Montenero, J. Non-Cryst. Solids 180 (1994) 51-57.
15. L. Baia, R. Stefan, W. Kiefer, J. Popp and S. Simon, J. Non-Cryst. Solids, 303 (2002), 379-386.
16. D.Streenivasu, V. Chandramouli, Bull Mater Sci 23(4) (2000) 281
17. L. Baia, T. Iliescu, S. Simon and W. Kiefer, J. Molec. Structure, 599, (2001), 9-13.
18. R. Capelletti, E. Colombi, G. Gnappi, P. Lottici, A. Montenero, inc. Proc. Int. Conf. on Defects in Insulating Crystals, Schloss Nord Kirchen, Germany 92.
19. A. Radu, L. Baia, W. Kiefer and S. Simon, Vibration. Spectroscopy, 39 (2005), 127- 130.
20. S. Hazra, A. Ghosh, Phys. Rev. B 51 (1995).

21. L. Baia, R. Stefan, J. Popp, S. Simon and W. Kiefer, J. Non-Cryst. Solids. 324 (2003), 109-117.
22. E. I. Kamitsos, Y. D. Yiannopoulos, M. A. Karacassides, G. D. Cryssikos, H. Jain, J. Phys. Chem. 100, (1997), 11755 - 11756.
23. L. Baia, W. Kiefer and S. Simon, Rom. Rep.Phys., 56, (3), (2004), 430-435.
24. P. Beneventi, D. Bersani, P. P. Lotici, L. Kovacs, F. Cordioli, A. Montenero, G. Gnappi, J. Non-Cryst. Solids, 192-193 (1995), 258-262.

STUDIA UNIVERSITATIS BABEŞ-BOLYAI, PHYSICA, LII, 2, 2007

ELECTRON DENSITY OSCILLATIONS IN ONE-DIMENSION FOR A CHAIN OF DENSE IMPURITIES

I. GROSU[*], L.TUGULAN[*]

ABSTRACT. Using the linear response theory we studied the Friedel oscillations in a one-dimensional noninteracting electron gas in the presence of a chain of dense impurities. The chain length is *l* and the impurities potential is assumed to be constant. The oscillations are strongly affected by the length of the impurities chain.

Keywords: One-dimensional electron gas, Many impurities, Constant potential, Friedel oscillations.

1. Introduction

The problem of the Friedel oscillations in a one-dimensional noninteracting gas, in the presence of a static impurity, was recently analyzed by Giuliani et al.[1] in order to give a correct analytical description of the induced density modulation. They pointed out that the original calculation [2] gave an incorrect answer. The model adopted in Ref.1 is based on the theory of linear response [3], and the impurity potential is assumed to be of the delta-function form. However, the simple delta-function potential (zero range potential) lacks one important feature that characterizes potentials, namely, the characteristic range and, as a consequence, the possibility of resonances [4]. A simple modification which introduces a finite range is a two-delta functions potential [5]. The importance of the Friedel oscillations was pointed out by Simon and Giuliani [6] in connection between their theoretical results and the scanning tunneling microscopy measurements. Another important effect of the Friedel oscillations was discussed by Zhitomirsky and Walker [7] in connection to the transition temperature in impure superconductors. More recently, the problem of the Friedel oscillations was discussed in nanostructures [8], and for the case of a quantum dot coupled to an edge of a disordered one dimensional wire [9]. Motivated by these important

[*] Department of Theoretical Physics, University of Cluj, 3400, Cluj, Romania

effects, we will analyze the problem of the Friedel oscillations in one dimension and in the presence of many impurities.

2. Model

In the following, we will consider the problem of the Friedel oscillations in the one-dimensional noninteracting electron gas and in the presence of many identical impurities. The distance between the adjacent impurities is *a*, and the impurities number is *n*. The length of the impurities chain is *l*=*na*. The distance *a* is assumed to be very small, that correspond to a dense chain of impurities. In this case the impurities potential will be assumed of the form:

$$V_{ext}(x)=\begin{cases} C; & 0\le x\le l \\ 0; & x<0, x>l \end{cases} \qquad (1)$$

where *C* is a constant that measures the strength of the potential. In order to find the distance dependence of the density, we will use the linear response theory (as in Refs.[1,3]). This dependence is given by:

$$n(x)=\int_0^\infty \frac{dq}{\pi}\chi(q)V_{ext}(q)\cos(qx) \qquad (2)$$

Here χ(*q*) is the static Lindhard function in one dimension (ħ=1):

$$\chi(q)=\frac{2m}{\pi\cdot q}\ln\left|\frac{2k_F+q}{2k_F-q}\right| \qquad (3)$$

(*m*-is the electron mass, and k_F - the Fermi wavevector). $V_{ext}(q)$ is the Fourier transform of the impurities potential:

$$V_{ext}(q)=\frac{C\cdot\sin(ql)}{q} \qquad (4)$$

Using Eqs.(3) and (4) in Eq.(2), and the new variable, $y=q/2k_F$, we find:

$$n(x) = \frac{mC}{\pi^2 k_F} \int_0^\infty \frac{dy}{y^2} \cdot \ln\left|\frac{1+y}{1-y}\right| \cdot \sin(2k_F l \cdot y) \cdot \cos(2k_F x \cdot y) \qquad (5)$$

With the help of the integral [10]:

$$\int_0^\infty \frac{dy}{y} \cdot \ln\left(\frac{b+y}{b-y}\right)^2 \cdot \cos(ay) = -2\pi \cdot si(ab), \qquad a > 0, b > 0 \qquad (6)$$

(where *si(x)* is the shifted sine-integral function), we obtain the following result:

$$\frac{d}{da_1} n(x) = -\frac{mC}{2\pi k_F} \left[si(b_1 + a_1) + si(b_1 - a_1)\right] \qquad (7)$$

where: $a_1 = 2k_F l$, and $b_1 = 2k_F x$. The large distance behavior in Eq.(7) can be obtained using the asymptotic behavior:

$$si(x) \sim -\frac{\cos(x)}{x} \qquad (8)$$

and we have:

$$\frac{d}{da_1} n(x) \cong \frac{mC}{\pi k_F b_1^2} \left[b_1 \cdot \cos b_1 \cdot \cos a_1 + a_1 \cdot \sin b_1 \cdot \sin a_1\right] \qquad (9)$$

From here it is easy to evaluate the large distances behavior of the density, as:

$$n(x) \cong \frac{mC}{\pi k_F} \cdot \frac{\sin(2k_F l) \cdot \cos(2k_F x)}{2k_F x} \cdot \left\{1 + \left[1 - 2k_F l \cdot \cot an(2k_F l)\right] \cdot \frac{\tan(2k_F x)}{2k_F x}\right\} \qquad (10)$$

In Figs.1-2 we plot the large distances dependence of the normalized density $R = n(x)/(mC/\pi k_F)$, for different values of the product $2k_F l$ (we take $2k_F = 1$).

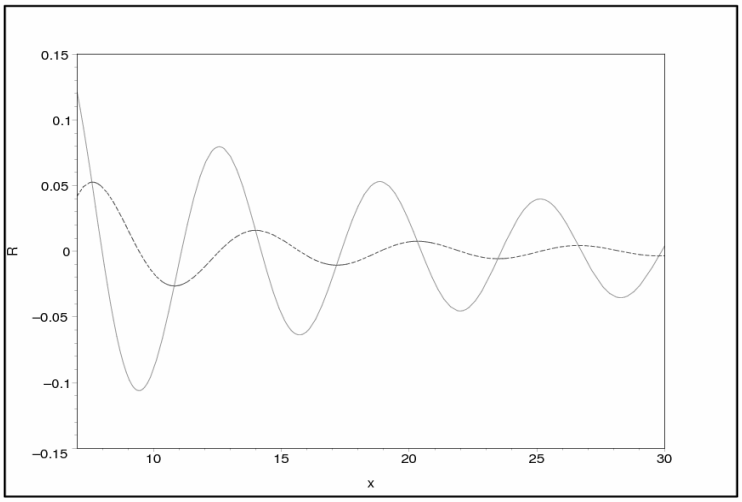

Fig.1 Distance dependence of the normalized density *R* for $2k_F = 1$, and for: a) $2k_F l = \pi/2$ (solid line), b) $2k_F l = \pi$ (dashed line)

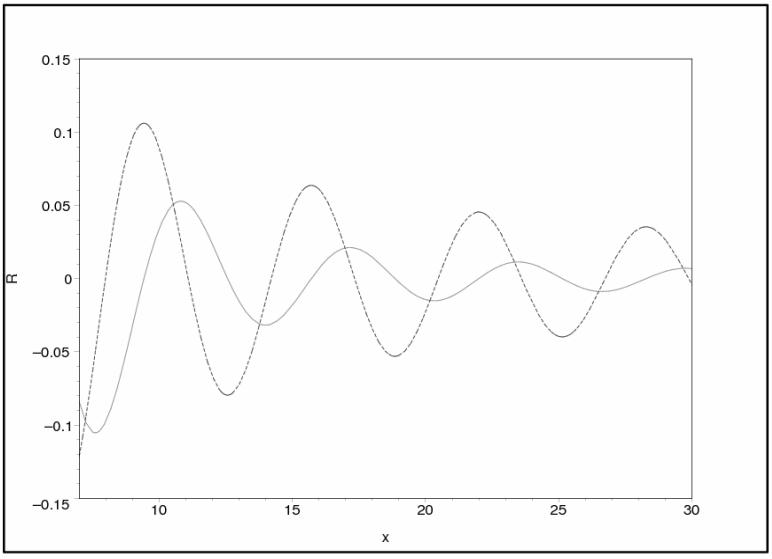

Fig.2 Distance dependence of the normalized density *R* for $2k_F = 1$, and for: a) $2k_F l = 2\pi$ (solid line), b) $2k_F l = 3\pi/2$ (dashed line)

The density oscillations (amplitudes and the positions of the maxima and the minima) are strongly affected by the length of the impurities chain.

3. Conclusions

In conclusion, we studied the problem of the Friedel oscillations in one dimension and in the presence of a dense chain of localized static impurities. The intermediate and large distance oscillations are strongly affected by the length of the impurities chain, connected to the compact form of the finite range potential. This effect is different from the mechanism proposed in Ref. [5], for two impurities both with a delta-function potential, where the interference effects affect the amplitudes, the maxima and the minima of the density oscillations. The behavior of the Friedel oscillations could be of interest in the study of the transition temperatures of some superconductors [11]. For the low dimensional superconductors, in the presence of the impurities, it was pointed out that the density variations near the impurity sites becomes important, for short coherence length superconductors, and can increase the transition temperature in the case of the s-wave superconductors [7]. The effect of the Friedel oscillations is also important in some nanostructured materials [8], and in the physics of the quantum dots systems [9].

REFERENCES

1. G.F.Giuliani, G.Vignale, T.Datta, Phys.Rev.B 72, 033411, (2005)
2. C.Kittel, "Solid State Physics", vol.22, edited by F.Seitz, D.Turnbull and H. Ehreinreich, Academic Press, New York, (1968)
3. G.E.Giuliani, G.Vignale, "Quantum Theory of the Electron Liquid", Cambridge University Press, Cambridge, (2005)
4. H.J.Lipkin, "Quantum mechanics", North-Holland, (1973)
5. I.Grosu, L.Tugulan, J.Supercond. (in press)
6. G.E.Simon, G.F.Giuliani, Phys.Rev.B 72, 045127, (2005)
7. M.E.Zhitomirsky, M.B.Walker, Phys.Rev.Lett.80, 5413, (1998)

8. Y.Hasegawa, M.Ono, Y.Nishigata, T.Nishio, T.Eguchi, J.Phys: Conf. Series 61, 399, (2007)
9. Y.Weiss, M.Goldstein, R.Berkovits, arXiv: 0704.1386 (cond-mat.)
10. I.S.Gradshteyn, I.M.Ryzhik, "Table of integrals, series, and products", Academic Press, (1980)
11. A.L.Fetter, Phys.Rev.140, A1921, (1965)